

Rest-frame Ultraviolet-to-Optical Properties of Galaxies at $z \approx 6$ and 5 in the Hubble Ultra Deep Field: from Hubble to Spitzer

Haojing Yan¹, Mark Dickinson², Daniel Stern³, Peter R. M. Eisenhardt³, Ranga-Ram Chary¹, Mauro Giavalisco⁴, Henry C. Ferguson⁴, Stefano Casertano⁴, Christopher J. Conselice⁵, Casey Papovich⁶, William T. Reach¹, Norman Grogin⁴, Leonidas A. Moustakas³, Masami Ouchi⁴

ABSTRACT

We use data from the first epoch of observations with the Infrared Array Camera (IRAC) on the *Spitzer* Space Telescope for the Great Observatories Origins Deep Survey (GOODS) to detect and study a collection of Lyman-break galaxies at $z \approx 6$ to 5 in the Hubble Ultradeep Field (HUDF), six of which have spectroscopic confirmation. At these redshifts, IRAC samples rest-frame optical light in the range 0.5 to $0.8\mu\text{m}$, where the effects of dust extinction are smaller and the sensitivity to light from evolved stars is greater than at shorter, rest-frame ultraviolet wavelengths observable from the ground or with the Hubble Space Telescope. As such, it provides useful constraints on the ages and masses of these galaxies' stellar populations. We find that the spectral energy distributions for many of these galaxies are best fitted by models of stellar populations with masses of a few $\times 10^{10} M_{\odot}$, and with ages of a few hundred million years, values quite similar to those derived for typical Lyman break galaxies at $z \approx 3$. When the universe was only 1 Gyr old, some galaxies had already formed a mass of stars approaching that of the present-day Milky Way, and that they started forming those stars at $z > 7$, and in some cases much earlier. We find that the lower limits to the space density for galaxies in this mass range are consistent with predictions from recent hydrodynamic simulations of structure formation in

¹Spitzer Science Center, California Institute of Technology, MS 220-6, Pasadena, CA 91125; yhj@ipac.caltech.edu

²National Optical Astronomy Observatory, 950 N. Cherry St., Tucson, AZ 85719

³Jet Propulsion Laboratory, 4800 Oak Grove Dr., Pasadena, CA 91109

⁴Space Telescope Science Institute, 3700 San Martin Dr., Baltimore, MD 21218

⁵Department of Astronomy, California Institute of Technology, Mail Code 105-24, Pasadena, CA 91125

⁶Steward Observatory, University of Arizona, 933 North Cherry Av., Tucson, AZ 85721

a Λ CDM universe. All objects in our samples are consistent with having solar metallicity, suggesting that they might have already been significantly polluted by metals and thus are not comprised of “first stars”. The values for dust reddening derived from the model fitting are low or zero, and we find that some of the galaxies have rest-frame UV colors that are even bluer than those predicted by the stellar population models to which we compare them. These colors might be attributed to the presence of very massive stars ($> 100M_{\odot}$), or by weaker intergalactic HI absorption than what is commonly assumed.

Subject headings: cosmology: observations — galaxies: evolution — galaxies: luminosity function, mass function — infrared: galaxies

1. Introduction

A striking result from studies of galaxy formation and evolution is that galaxies as massive as $\sim 10^{11}$ – $10^{12}M_{\odot}$ existed at $z \approx 1$ or even out to $z \approx 2$ (e.g., Fontana et al. 2004, Cimatti et al. 2004, Glazebrook et al. 2004, Daddi et al. 2005), and galaxies with masses $\sim 10^{10}M_{\odot}$ are already rather commonly seen at $z \approx 3$ (e.g., Papovich, Dickinson & Ferguson 2001; Shapley et al. 2001). Many such massive galaxies apparently have well-evolved stellar populations, *i.e.*, they must have formed their stars well before the epoch at which they are observed. For example, about 20% of the LBGs in the $z \approx 3$ sample of Shapley et al. (2001) have stellar masses $\geq 10^{10}M_{\odot}$ and inferred ages > 1 Gyr, implying formation redshifts of $z_f > 5$. Infrared selected samples have identified candidates for more massive, evolved galaxies at $z \approx 2$ – 3 (Franx et al. 2003; Yan et al. 2004; Labbé et al. 2005), with inferred stellar masses that can exceed $10^{11}M_{\odot}$. The dominant luminosity components for some of these objects are best explained by an old stellar population with ages of 1.5–2.5 Gyr, which, taken at face value, suggests that they formed no later than $z_f = 5$, and possibly as early as $z_f = 15$ – 20 .

If the inferences from these studies are correct, we should see massive galaxies at $z \approx 5$ and beyond. One of the central science drivers of the Great Observatories Origins Deep Survey (GOODS) *Spitzer* Legacy Science Program is to constrain the stellar masses of L^* galaxies out to $z \approx 5$ with the rest-frame near-IR observations made by the Infrared Array Camera (IRAC; Fazio et al. 2004). In fact, the performance of this instrument in its 3.6 and $4.5\mu\text{m}$ channels exceeds the pre-launch expectations because the in-flight point spread function (PSF) exceeds the telescope specifications. This enables the detection of galaxies as distant as $z \approx 6$. At these redshifts, the observed optical and near-infrared data sample rest-frame ultraviolet light, which is sensitive to young star formation and dust absorption, but

which gives relatively little information about the age or mass of a galaxy’s stellar population. *Spitzer* and IRAC offer access to the rest-frame optical light which is less subject to dust extinction and more sensitive to the longer-lived stars that dominate the stellar mass. Egami et al. (2005) have used IRAC to detect a galaxy at $z \approx 6.7$ lensed by a foreground cluster, while Eyles et al. (2005) have studied two galaxies at $z \approx 6$ that are detected in the GOODS IRAC data. In both papers, the spectral energy distributions were used to estimate the stellar masses of these galaxies, and to demonstrate the presence of stars formed several tens to several hundred million years earlier.

In this paper, we study the rest-frame UV to optical photometry of $z \approx 6$ and 5 (hereafter “high- z ”) galaxies selected from the Hubble Ultra Deep Field (HUDF¹; PI. S. Beckwith), using the HST ACS/NICMOS data and the first epoch of GOODS IRAC observations of the *Chandra* Deep Field South (CDF-S). While the GOODS IRAC data cover a much wider area, an important advantage of analyzing galaxies in the HUDF is the availability of very deep near-infrared imaging, in two bands, from HST/NICMOS (Thompson et al. 2005) for a significant number of objects. Without such data, there is rather little constraint on the rest-frame ultraviolet properties of galaxies at $z \gtrsim 5$ compared to what other studies have had available when analyzing Lyman-break galaxies at lower redshifts. The UV luminosity of a galaxy is an important constraint on its rate of on-going star formation, while the UV spectral slope is sensitive to dust reddening. When fitting population synthesis models to galaxy photometry, it is important to have constraints on both of these quantities in order to derive reliable star formation rates, extinction, stellar population ages, and mass-to-light ratios. At $z \approx 6$, flux in the ACS i_{775} band, and to a lesser extent also the z_{850} -band (depending on the galaxy redshift), is suppressed by the stochastic effects of the Lyman α forest. The ACS bands alone are insufficient for reliably measuring the UV luminosity of $z \approx 6$ galaxies, and the UV slope cannot be constrained without redder bandpasses. At $z \approx 5$, the z_{850} band gives a reliable luminosity at $\sim 1500\text{\AA}$, but the spectral slope is again unconstrained without near-infrared data. These high-redshift galaxies are extremely faint, and only the brightest are detected even in the very deep near-infrared data available for the GOODS project from ISAAC on the VLT, and even then at fairly low signal-to-noise ratios. The NICMOS HUDF data are much deeper and detect all galaxies from our sample that fall within their field of view, providing two more photometric bands that cleanly constrain the UV luminosity and spectral slope.

The paper is organized as follows. The high- z galaxy samples are briefly described in §2, and the IRAC counterparts of these galaxies are discussed in §3. The stellar population

¹See <http://www.stsci.edu/hst/udf>

synthesis models that we use to fit the observed spectral energy distributions (SEDs) of these galaxies are described in §4. The constraints on the stellar populations at $z \approx 6$ and 5 are given in §5 and 6, respectively. We briefly compare our results with recent hydrodynamic simulations in §7, and conclude the paper with a summary in §8. We denote the F435W, F606W, F775W, and F850LP bands of ACS as B_{435} , V_{606} , i_{775} , and z_{850} , respectively, and the F110W and F160W bands of NICMOS as J_{110} and H_{160} , respectively. In one occasion we also use the K_s -band photometry obtained by the ISAAC instrument at the VLT. All magnitudes are in the AB system. Throughout this paper, we adopt the following cosmological parameters based on the Wilkinson Microwave Anisotropy Probe result (WMAP) from Spergel et al. (2003): $\Omega_M = 0.27$, $\Omega_\Lambda = 0.73$, and $H_0 = 71 \text{ km s}^{-1} \text{ Mpc}^{-1}$ ($h = 0.71$).

2. Samples of Galaxy Candidates at $z \approx 6$ and 5 in the HUDF

The sample of $z \approx 6$ galaxy candidates used in this paper is from Yan & Windhorst (2004; hereafter YW04), which consists of 108 objects to $z_{850} \leq 30.0$ mag. These candidates were selected as i_{775} -band dropouts using the criteria of (1) $(i_{775} - z_{850}) \geq 1.3$ mag and (2) non-detection in both the B_{435} and the V_{606} bands ($S/N < 2$). These criteria are similar to those used in Dickinson et al. (2004). The targeted redshift window is $5.5 \lesssim z \lesssim 6.5$. There are 6 multiple systems among these candidates (see Table 1 of YW04), where a multiple system is defined as a group whose members are within $1''$ of each other. Such a multiple system cannot be resolved by IRAC, and will show up as a single IRAC source if detected.

The sample of $z \approx 5$ galaxy candidates is the V_{606} -band dropout sample of Yan et al. (in preparation). Briefly, the selection criteria are (1)

$$\begin{cases} (V_{606} - i_{775}) > 1.2, & \text{if } (i_{775} - z_{850}) \leq 0.3 \\ (V_{606} - i_{775}) > 0.4 + 2.67 \times (i_{775} - z_{850}), & \text{if } 0.3 < (i_{775} - z_{850}) \leq 0.6 \\ (V_{606} - i_{775}) \geq 2.0, & \text{if } (i_{775} - z_{850}) > 0.6 \end{cases}$$

and (2) non-detection in the B_{435} band ($S/N < 2$). These criteria are similar to those of Giavalisco et al. (2004b), but are fine-tuned to better suit the high S/N HUDF data, which have a tighter low-redshift galaxy locus in the color space. The targeted redshift window is $4.5 \lesssim z \lesssim 5.5$. This sample consists of ~ 550 candidates, among which 95 objects form 43 multiple systems.

3. IRAC Counterparts to High- z Galaxy Candidates

The IRAC data used in this paper are the mosaics of the first epoch of GOODS observations of the CDF-S². These data are discussed in detail in Dickinson et al. (in preparation), and are also briefly described in Yan et al. (2004). To summarize, the middle one-third of the GOODS CDF-S field, which includes the HUDF, has been observed in all four IRAC channels with a nominal exposure time of ~ 23.18 hours per pixel. The final drizzle-combined mosaics have a pixel scale of $0.6''$, or approximately half of the native IRAC pixel size. These IRAC mosaics are registered to the same astrometric grid as the GOODS ACS images of the same area, which is also the astrometric frame of the ACS HUDF. Sources were detected in a weighted sum of the $3.6\mu\text{m}$ and $4.5\mu\text{m}$ images. The IRAC photometric catalogs used here are somewhat different from those used in Yan et al. (2004) in the sense that the source extraction parameters for the current catalogs are better tuned for deblending objects.

3.1. Matching high- z objects in the IRAC images

As the FWHM of the PSF in the $3.6\mu\text{m}$ channel is about $1.8''$, the matching of the high- z galaxy candidates and the IRAC sources was done with a generous, $2''$ search radius. The matched sources were then visually inspected to ensure that the identifications were secure. While the rate of the mis-identification depends on a number of factors (such as the brightness of both the source and its neighbours, and their proximity), we found that roughly one-fourth of the identifications in our sample matched unrelated objects. These false identifications were thus rejected. Furthermore, we limit our study only to the most reliable identifications. In order to avoid ambiguity in interpreting the measured fluxes, we do not include any sources that are blended with foreground objects. Neither do we include any sources that are fainter than $m_{3.6\mu\text{m}} = 26.4$ mag (the formal $S/N = 5$ limit for isolated point sources in the $3.6\mu\text{m}$ channel). In practice, all but two of the matched objects have $m_{3.6\mu\text{m}} \leq 25.3$ mag.

Because of the precise alignment of the IRAC mosaics to the GOODS ACS images, the securely matched IRAC sources always have centroids within $0.6''$ from the centroids as measured in the ACS images³. In total, seven $z \approx 6$ objects (in 3 multiple systems) and twenty-two $z \approx 5$ candidates (3 single objects and 8 multiple systems) were securely matched

²See http://data.spitzer.caltech.edu/popular/goods/20041027_enhanced_v1.

³The astrometric accuracy, which is based on brighter point sources, is always good to $0.2''$ in all channels.

with IRAC sources⁴. Since none of the multiple systems is resolved by the IRAC images, from now on we will not distinguish whether an IRAC source is a multiple system or a single object, and will simply call it an “object”⁵. Therefore, our IRAC-detected high- z sample consists of three $z \approx 6$ objects and eleven $z \approx 5$ objects. Among them, two of the $z \approx 6$ galaxies and three of the $z \approx 5$ galaxies have been spectroscopically confirmed (Dickinson et al. 2004; Stanway et al. 2004; Malhotra et al. 2005; Stern et al., in preparation; see §3.4). All the objects in our sample are clearly detected in $3.6\mu m$, and some of them are detected in $4.5\mu m$ as well, where the data are somewhat shallower. The background noise is substantially larger and the PSF broader in the $5.8\mu m$ and $8.0\mu m$ IRAC channels, and none of the galaxies is significant detected at those wavelengths. ACS and IRAC image cutouts (and, where available, NICMOS as well) are displayed in Fig. 1 and 2 for the the $z \approx 6$ and $z \approx 5$ galaxies, respectively.

Perhaps unsurprisingly, these IRAC-detected objects are also some of the optically brightest galaxies in the ACS high- z sample. The faintest z_{850} -band magnitude of the three $z \approx 6$ sources is 26.88 mag (#7ab after adding the fluxes from its two members; detailed in §3.2), while the faintest i_{775} -band magnitude of the eleven $z \approx 5$ sources is 26.74 mag (#48ab after combining its two members). Six objects with $z_{850} < 26.9$ in the $z \approx 6$ sample, and 19 objects with $i_{775} < 26.9$ in the $z \approx 5$ sample, are not included in the present analysis. Only the faintest $z \approx 6$ object and the three faintest $z \approx 5$ objects are certainly not detected in the $3.6\mu m$ IRAC data at the 2σ level. The others are not included because they are blended with other, nearby IRAC sources and were thus rejected during visual inspection regardless of whether they were detected.

3.2. Photometry

When studying SEDs measured by different instruments at widely separated wavelength ranges, one of the largest challenges is to measure a consistent fraction of the light from each object in each passband such that the spectral energy distribution is reliable. In our case, we utilize matched-aperture photometry as much as possible (using SExtractor of Bertin & Arnouts 1996), and choose to bring the measurements as close to the total magnitudes as possible. Our current best-effort photometry of these IRAC-detected $z \approx 6$ and 5 galaxy

⁴While there seems to be a larger fraction of multiple systems than single objects, we have not yet found sufficient evidence that IRAC preferably identified multiple systems.

⁵For these multiple systems, we emphasize that they satisfy our high- z color selection criteria either when counting their components individually or when combining the components as a whole.

candidates is given in Table 1 and 2, respectively.

For the $z \approx 6$ candidates, the ACS magnitudes (i_{775} and z_{850}) are taken from YW04, which are SExtractor “MAG_AUTO” magnitudes measured through matched apertures using the z_{850} mosaic as the detection image. The ACS magnitudes (V_{606} , i_{775} and z_{850}) of the $z \approx 5$ candidates are also “MAG_AUTO” values, but were obtained using the i_{775} mosaic as the detection image. For the multiple systems (which are not resolved by either the NICMOS images or the IRAC images), their combined magnitudes are listed as well.

For those sources that are detected in the NICMOS HUDF images, their J_{110} and H_{160} magnitudes are based on the NICMOS vs. ACS color indices measured through matched apertures using re-binned ACS mosaics as the detection images. The high-resolution ($0.03''/\text{pixel}$) ACS mosaics were first block-averaged by 3×3 to the resolution of the NICMOS mosaics ($0.09''/\text{pixel}$), and then registered to the NICMOS mosaics⁶. SExtractor was run using the degraded z_{850} image and i_{775} image as the input detection images to extract the NICMOS vs. ACS colors for the $z \approx 6$ and $z \approx 5$ objects, respectively. These color indices were then added to the z_{850} (i_{775}) magnitudes to obtain the final NICMOS magnitudes listed in Table 1 (2).

Because the angular resolution of the IRAC images is approximately 10-20 \times broader than that of the HST NICMOS and ACS images, simple rebinning and matched aperture photometry is not applicable, and a different method must be used. The GOODS IRAC images are very deep, and crowding by neighboring objects can be a problem for photometry, even for objects selected to be relatively isolated, like our high- z sample. We minimize this by using small apertures ($3''$ diameter) and a correction to total flux. The aperture corrections were derived from extensive Monte Carlo simulations in which artificial galaxies with varying magnitudes and sizes were inserted into the images and then detected and measured using the same SExtractor cataloging parameters used for the real data. Because our objects are compact, we apply aperture corrections derived for simulated galaxies with half-light radii $< 0''.5$, which average -0.55 mag and -0.60 mag for the $3.6\mu\text{m}$ and $4.5\mu\text{m}$ channels, respectively. The corrected aperture magnitudes for IRAC are given in Tables 1 and 2.

In addition to the ACS, NICMOS and IRAC data, we also use the deep VLT/ISAAC K_s -band images (Vandame et al., in preparation; Giavalisco et al. 2004a). Only one object, #6ab in the $z \approx 5$ sample, is significantly ($S/N > 3$) detected. While the inclusion or exclusion of this data point is not significant for this object in particular, we use it for the sake of completeness.

⁶We used the “rotated” (North-up and East-left) NICMOS images included in the version 1.0 public data release made by the NICMOS HUDF team on March 9, 2004.

3.3. Assessment of systematic errors in photometry

The systematic errors in IRAC photometry are largely caused by the source blending. To estimate such systematic errors, we used two more methods to estimate the IRAC magnitudes of these sources. While none of these methods (including the aperture photometry) completely eliminates the contamination caused by blending, they are affected differently. By comparing these three different kinds of magnitudes, we can estimate the effect of contamination to these sources.

One of the additional estimates is the usual “MAG_AUTO” magnitude measured by SExtractor. The other one is based on point spread function (PSF) fitting, which is justified by the fact that these sources are very nearly point sources at IRAC’s resolution. The centroids of the sources measured from the ACS images are used as priors to the fitting algorithm. The total fitted magnitude of a multiple system is based on the sum of the fitted fluxes of the individual components. We use the root-mean-square (rms) dispersion of the three types of magnitudes as a measure of the systematic plus random measurement errors in these crowded images. The zeropoint calibrations for IRAC are believed to be accurate at the 10% level or better, but we allow for additional systematic uncertainty in the absolute photometry at this level, and therefore add (by simple summation because it is a systematic term) an additional 0.1 mag to obtain the final error estimates for these objects (Tables 1 and 2).

For the ACS and the NICMOS photometry, we assess the possible systematic errors by comparing our results against those of others. We use the catalogs included in the HUDF ACS and NICMOS data release (hereafter “the public catalogs”) as well as other published results in the literature for this comparison. We put the emphasis on the comparison of colors because they play a more important role than anything else in the SED analysis. Given the different source extraction procedures in the different studies, colors are also the most robust metric for such a comparison.

Since the public ACS catalog is largely an i_{775} -band-based catalog (*i.e.*, the i_{775} -band image was used to detect sources and to define source extraction apertures), we only compare the photometry of the $z \approx 5$ sources. Object #10 and #14ab are excluded from this comparison because they are not in the public ACS catalog.

For the majority of these sources, both the $(V_{606} - i_{775})$ and $(i_{775} - z_{850})$ indices agree to within 0.1 mag in these two catalogs. Given that the two catalogs use different flavors of magnitude (the ACS public catalog uses SExtractor “MAG_ISO” while ours uses “MAG_AUTO”), and that most of the sources have irregular morphologies, such an agreement is reasonable, and the size of the discrepancies reflects the impact of choosing different

photometric apertures.

There are three sources whose ($V_{606} - i_{775}$) colors differ by > 0.1 mag, namely, #4ab, 15ab and 48ab. Such discrepancies are mainly caused by the large photometric errors in the V_{606} -band, and can be explained by the random errors (*i.e.*, those derived based on the S/N of the sources) associated with these colors. Only #15ab has ($i_{775} - z_{850}$) different by > 0.1 mag. Our measurement gives an index of 0.13 ± 0.04 mag, while the ACS public catalog gives 0.28 ± 0.03 mag. This very irregular object has also been studied in detail by Rhoads et al. (2005), who used different isophotal apertures on a slightly different version of the HUDF images. Those authors give an even more different value of ($i_{775} - z_{850}$) = 0.47 ± 0.02 mag (after combining their “core” and “plume” components). We believe that the discrepancies of different results can also be attributed to the different choices of photometric apertures and the contamination from the two physically unrelated close neighbors.

The means of the color index differences are 0.01 ± 0.12 mag and 0.02 ± 0.08 mag for ($V_{606} - i_{775}$) and ($i_{775} - z_{850}$), respectively. The useful quantities are the dispersions, which tell us how these colors can be different because of the systematic errors in their photometry. Given the V_{606} -dropout nature of these sources, it is reasonable to assume that the errors in both i_{775} and z_{850} are comparable, while those in V_{606} are larger. Therefore, we assign these sources additional errors of 0.056 mag to both i_{775} and z_{850} , and 0.106 mag to V_{606} , respectively. These numbers, while added in quadrature, give the corresponding values of dispersion in the relevant colors. For the $z \approx 6$ objects, we assume that their ($i_{775} - z_{850}$) colors suffer a comparable amount of systematic error as the ($V_{606} - i_{775}$) colors of the $z \approx 5$ sources. Thus we assign them additional errors of 0.106 mag to i_{775} , and 0.056 mag to z_{850} , respectively. The errors reported in Table 1 and 2 are the sum of such additional systematic error estimates and the random errors based on their S/N .

We compare our ($i_{775} - z_{850}$) colors of the three $z \approx 6$ sources to the values (based on a fixed-size, $0.5''$ -diameter aperture) reported in Bunker et al. (2004), and find that the differences can all be explained by the systematic uncertainties that we adopt.

Since our NICMOS magnitudes are derived based on matched-aperture photometry between ACS and NICMOS, we believe those magnitudes are superior to any others for the purpose of SED analysis. As these magnitudes are calculated by adding NICMOS vs. ACS colors to the ACS magnitudes (*i.e.*, adding $J_{110} - i_{775}$ or $H_{160} - i_{775}$ to i_{775} for $z \approx 5$ objects, and adding $J_{110} - z_{850}$ or $H_{160} - z_{850}$ to z_{850} for $z \approx 6$ objects), these values should “inherit” the systematic errors of the ACS magnitudes. Therefore, we assign an additional error of 0.056 mag to both bands. Compared to our photometry, the “MAG_AUTO” values in the NICMOS public catalog (version 1.0) on average are fainter by 0.12 mag in J_{110} and 0.24 mag in H_{160} , respectively. The NICMOS photometry of the three $z \approx 6$ objects has also been

discussed by Stanway et al. (2004), and their values agree to ours to within the quoted errors (0.1–0.2 mag). Rhoads et al. (2005) also discussed the NICMOS colors of object #15ab in our $z \approx 5$ sample; while their $J_{110} - H_{160}$ colors are bluer by 0.19 mag as compared to our measurements, such a difference can still be understood if we consider the quoted errors.

3.4. Galaxies with confirmed redshifts

Two objects in the $z \approx 6$ sample have spectroscopic redshift measurements. Object #1 was observed with the Keck and VLT observatories and with the ACS grism, and has $z = 5.829$ (Dickinson et al. 2004; Stanway et al. 2004; Vanzella et al. 2005). Based on its morphology, the secondary component #1b seems to be a “filament” extending from #1a (see Fig. 1), and therefore it is taken as at the same redshift as #1a.

The Grism ACS Program for Extragalactic Science (GRAPES; Pirzkal et al. 2004a) has confirmed the high- z nature of #5abc (Malhotra et al. 2005). However, the components #5ab (not resolved by the GRAPES; ID 3450) and #5c (ID 3503) are identified at rather different redshifts of 5.9 and 6.4, respectively. As their contributions to the IRAC fluxes cannot be separated, as a first-order approximation we treat them as at the same, but not-yet-determined redshift. We will return to the discussion of the redshift of this system in §5.1 again.

Four objects in the $z \approx 5$ sample have spectroscopic redshifts. Object #6ab, 7ab and 15ab have been observed at Keck and are confirmed to be at $z = 4.65$, 4.78 and 5.49, respectively (Stern, in preparation). The GRAPES has also measured $z = 4.88$ and 5.52 for #7ab and 15ab, respectively (Xu et al. 2005; see also Rhoads et al. 2005 for an initial identification of #15ab, which gave $z = 5.42$ for this source). Here we adopt the values obtained at Keck. The GRAPES has also measured $z = 5.05$ for object #4ab (Xu et al. 2005), which we adopt in our discussion.

4. Overview of Stellar Population Synthesis Models and Procedures

We use the stellar population synthesis models of Bruzual & Charlot (2003; BC03) to analyze the SEDs of these IRAC-detected high- z galaxies. For ease of comparison with other studies, we use a Salpeter (1955) initial mass function (IMF). This IMF is incorporated in BC03 models with lower and upper mass cut-offs at 0.1 and 100 M_{\odot} , respectively. Recent work has favored a flatter IMF below 1 M_{\odot} (e.g., Chabrier, 2003). For our purposes, the shape of the IMF at low masses only affects the derived stellar mass-to-light ratios (M/L)

in a way that is nearly independent of stellar population age. The Chabrier IMF yields masses that are 0.53–0.60 times those derived using a Salpeter IMF; the same will be true for galaxies at lower redshifts to which we might compare our results for the high-redshift population. Instead, changing the slope or shape of the IMF at high masses can have more pronounced effects on galaxy colors and their time evolution, and on the relative mass-to-light ratio as a function of stellar population age. E.g., a top-heavy IMF will produce more light and have smaller M/L at younger ages, and the luminosity fade more quickly with time. As yet, we have little or no observational constraint on the IMF for galaxies at $z \approx 5$ to 6, and we therefore adopt the Salpeter form to simplify comparison with other published work, but systematic uncertainties related to the choice of the IMF should be kept in mind. We will return briefly to one IMF-related issue in Sections 5.2 and 6.2.

The model spectra generated by the BC03 code are shifted across the range of expected redshifts with a step size $\Delta z = 0.1$, and attenuated by intergalactic HI absorption according to the recipe of Madau (1995). The model spectra are then integrated through the bandpass response curves and compared to the observations. We consider BC03 models with five metallicities Z , from $Z_{\odot}/200$ to solar. We explore a variety of star formation histories (SFHs): instantaneous bursts (or simple stellar populations, SSPs); continuous but exponentially declining star formation with e-folding timescales from $\tau = 10$ Myr to 1 Gyr; and continuous star formation at a constant rate. We also consider dust reddening following the empirical law of Calzetti et al. (2000) within the range of $E(B - V) = 0$ –2.3 mag. An important constraint on the models is that the inferred ages should not exceed the age of the universe at the corresponding redshifts. For example, if a set of models give photometric redshift of $z_p = 6.0$ for an object, the legitimate models should only be those that have ages less than 0.95 Gyr (the age of the universe at $z = 6$ in our adopted cosmology).

In some cases, the observed photometry cannot be satisfactorily fit by a single-component model of the sorts that we have considered. One reason why this may occur is because the real SFH is likely more complicated than these basic models. Therefore, we consider the superposition of two models when a single model fails to explain the observed SED. This “two-component” approach has been used by Yan et al. (2004) to explain the weak optical fluxes of the IRAC-selected extremely red objects (IEROs). It is similar to the “maximum M/L ” method of Papovich, Dickinson & Ferguson (2001), where they derived the maximum stellar mass allowed by the observed SED of a given galaxy through breaking its light into the contributions from a maximally old component (formed at $z_f = \infty$) and from a young component. The differences between the two methods are that introducing one more component in our current approach is driven by what is necessary (*i.e.*, when the one-component models fail) rather than what is allowed, and that each of the two components can be formed at any arbitrary z_f as long as it is larger than the redshift at which a given galaxy is observed. This

approach is also similar to that of Berta et al. (2004), but is different in the sense that they considered an arbitrary large number of components represent by SSPs, while we limit our method to only two components (but not necessarily SSPs) such that the major processes can be seen more clearly.

We carry out the fitting in flux density units (instead of magnitudes), and minimize χ^2 to find the best-fitting model. When only single-component models are involved, the possible free parameters are: redshift (z), age (T), stellar mass (M), star formation history (τ ; SSP is treated as $\tau = 0$), reddening ($E(B - V)$), and metallicity (Z). When a spectroscopic redshift is available, this parameter is fixed. When two-component models have to be evoked, we require both components be at the same redshift and have the same metallicity.

In the practice of minimizing χ^2 , the goodness-of-fit is usually measured by the reduced- χ^2 , which is defined as $\chi'^2 = \chi^2/\nu$, where ν is the degrees of freedom of the given problem. In our case, ν is the number of available bandpasses minus the number of free parameters. The objective of our analysis is not only to find the parameters that best describe the SEDs (*i.e.* the ones giving the smallest χ'^2), but also to find the ranges within which the parameters can still give satisfactory fits to the SEDs (*i.e.*, the ones giving acceptable χ'^2). While in principle the latter can be achieved by drawing constant χ^2 boundaries as confidence limits on the estimated parameters, in practice it is difficult to take this approach. The fundamental difficulty is that the number of available bandpasses is limited, and thus for most of objects in our samples the values of ν would be zero or negative if we were to vary all the parameters.

To overcome this difficulty, we take the following approach. For a given object, we carry out the fitting procedure in separate runs, and require $\nu \geq 1$ in each run. This is achieved by “freezing” different parameters in different runs separately. Whenever possible, we simultaneously fit for the maximum number of free parameters allowed, *i.e.*, making $\nu = 1$. For example, for an object that has five bands available, we can fit for four free parameters at the same time if using single-component models. A possible run then can fit for (T, M, z, Z) with $(\tau, E(B - V))$ fixed, or (T, M, z, τ) with $(Z, E(B - V))$ fixed, and so on. We start from an arbitrary combination of maximum number of free parameters (but always including T and M , and also z if it is unknown), and find the best solution in this run. Of course, this requires we fix other parameters to some initial values based on our best-guess. We deem a fit to be of high quality if it has $\chi'^2 \leq 1 + \sqrt{2/\nu}$ (Press et al. 1992). When $\nu = 1$, which is true for most cases, this criterion is $\chi'^2 \leq 2.41$. If the best-fit in this run is a high-quality solution, we then “freeze” the parameters (anything other than T and M) to the values of this best-fit, and begin finding the best-fit in a different run involving a combination of different parameters. We repeat this process until all free parameters are exhausted, and then declare the best solution in the last run as the best-fit model to the

object under question. Finally, we alter all the parameters around the best-fit values and see to what extent we can still obtain high-quality fits. This approach has a number of caveats, one being that such a solution might be a local best-fit but not a global best solution. Here we have to neglect such possible caveats.

5. Stellar populations at $z \approx 6$

Here we discuss in detail the fitting results for the three objects in the $z \approx 6$ sample. The passbands that go into the fitting procedure are from i_{775} to $3.6\mu\text{m}$ (see Table 1). The best-fit models are shown in Fig. 3, and their parameters are summarized in Tab. 3.

5.1. Evidence of evolved, massive systems

We discuss the three $z \approx 6$ objects in order of easiness in their fitting.

Object #7ab: This object can be fitted by single-component models. The best-fit model ($\chi'^2 = 0.66$) to this object is a short burst ($\tau = 10$ Myr) at $z_p = 5.9$, with solar metallicity and no reddening. The derived age is 0.1 Gyr and the stellar mass is $4.7 \times 10^9 M_\odot$. Around this best-fit, we find following constraints on the free parameters:

(1) τ : At $0 \leq \tau \leq 10$ Myr (including SSP), we can find high-quality solutions of the same quality ($\chi'^2 < 0.7$) as the best-fit, and the derived age and mass are also effectively the same. The quality of fit is rapidly reduced at $\tau > 10$ Myr, although it does not seem to depend on τ in a linear fashion. We are able to find high-quality solutions sporadically with increasing τ all the way to $\tau \leq 70$ Myr, and if introducing $E(B - V) \approx 0.2$ mag such solutions can still be found until $\tau \leq 0.1$ Gyr. Such solutions with $\tau > 10$ Myr, however, seem unstable, as changing their ages (T) by only one step in either direction will immediately make $\chi'^2 > 5$.

(2) Z : While lowering metallicities always (although non-linearly) gives at least two-times worse χ'^2 , we cannot reject sub-solar metallicities at a significant level. Such models generally produce an older age and a larger mass.

(3) $E(B - V)$: The quality of fit becomes significantly worse if $E(B - V) > 0$. At $E(B - V) = 0.23$ mag, any solution has χ'^2 at least twice as bad as the best fit. If $E(B - V) \geq 0.45$ mag, no high-quality solution can be found.

(4) T & M : We find high-quality solutions only within $0.05 \leq T \leq 0.1$ Gyr and $1.4 \times 10^9 < M < 1.8 \times 10^{10} M_\odot$.

We do not find any acceptable single-component models to fit object #1ab and 5abc. The best-fit single-component models to #1ab and 5abc have $\chi'^2 = 10.49$ and 2.78, respectively, and none of them satisfy the high-quality criterion ($\chi'^2 \leq 2.41$ in these cases) that we adopted. For the sake of completeness, we list the parameters of these fits: ($T = 0.9$ Gyr, $\tau = 0.9$ Gyr, $M = 1.9 \times 10^{10} M_\odot$, $E(B - V) = 0$, $Z = 0.2Z_\odot$) for #1ab, and ($T = 0.9$ Gyr, $\tau = 0.5$ Gyr, $M = 1.6 \times 10^{10} M_\odot$, $E(B - V) = 0$, $Z = 0.2Z_\odot$) for #5abc. Note that both models have a very old age of 0.90 Gyr (the age of the universe at $z = 5.8$ and 5.9 is 0.99 and 0.97 Gyr, respectively), which means that one has to push the single-component models almost to their limits in order to obtain even these mediocre fits.

Therefore, we have to consider two-component models for these two objects. From here on, we use subscripts “E” (evolved) and “Y” (young) to denote the parameters for the primary and secondary components, respectively. As we require both components have the same redshift and metallicity (see §4), no subscript is put to these two parameters.

Object #5abc: The best-fit ($\chi'^2 = 0.23$) to this object has $z_p = 5.9$ and $Z = Z_\odot$, and ($T_E = 0.9$ Gyr, $\tau_E = 0.2$ Gyr, $M_E = 3.8 \times 10^{10} M_\odot$, $E(B - V)_E = 0$) and ($T_Y = 0$, $M_Y = 1.0 \times 10^8 M_\odot$, $E(B - V)_Y = 0$), respectively. We note that its photometric redshift is consistent with the redshift given by the ACS grism (Malhotra et al. 2005; $z = 5.9$) for the component #5ab. Excluding the contribution of #5c (see §3.3) from the SED does not change any of our conclusions.

(I) High-quality solutions can only be found when the young component has $T_Y \leq 30$ Myr and $E(B - V)_Y = 0$. Its τ_Y , however, is arbitrary, because any SFH gives effectively the same solution at such a young age. For the same reason, this component does not pose any constraint on the metallicity.

(II) If we assume that both components have the same reddening, *i.e.*, $E(B - V)_E = 0$, we have following constraints on the primary component:

(1) τ & T : High-quality solutions are available only when $\tau_E \leq 0.4$ Gyr and $T_E \geq 0.4$ Gyr. Thus the age implies a formation redshift $z_f \gtrsim 8.9$. The youngest T_E (0.4 Gyr) is found only when $\tau_E \leq 80$ Myr. If $0.2 \lesssim \tau_E \lesssim 0.4$ Gyr, the youngest T_E will be 0.7 Gyr, implying $z_f \gtrsim 16$.

(2) M : We find high-quality solutions only when $1.3 \times 10^{10} \lesssim M_E \lesssim 6.2 \times 10^{10} M_\odot$.

(3) Z : At one-step lower metallicity, $Z = 0.4Z_\odot$, solutions of comparable high quality are available. Decreasing metallicity beyond this value steadily decreases the quality of fit, and no high-quality solutions can be obtained if $Z = 1/200Z_\odot$ (the lowest metallicity available in BC03).

(III) If non-zero $E(B - V)_E$ is allowed (*i.e.*, the two components can have different reddening), most of the parameters for the primary component are no longer well constrained. Even in this case, however, the stellar mass is $M > 2.0 \times 10^{10} M_\odot$ for high-quality solutions. We note that none of the solutions with non-zero $E(B - V)_E$ has as small χ'^2 as the best-fit model does. If we confine the solutions to solar metallicity, no high-quality solution can be found at $E(B - V)_E \gtrsim 1.1$ mag. This constraint is largely set by the slope of the SED from $3.6\mu\text{m}$ to $4.5\mu\text{m}$ (larger reddening values would require a much steeper slope). We find that most of the high-quality solutions have $E(B - V)_E \lesssim 0.45$ mag if $Z = Z_\odot$, which might indicate that the true reddening value is indeed insignificant. For low reddening values, the high-quality solutions quickly converge to those obtained with $E(B - V)_E = 0$.

Object #1ab ($z = 5.83$):⁷ We find no satisfactory one- or two-component model fit to this object if we adopt the normal standard of high-quality. As we will discuss in detail in the next section, we find that the large χ'^2 values are mainly caused by its abnormal ($z_{850} - J_{110}$) color as compared to the BC03 models. This suggests that the models used for the secondary (young) component might have some intrinsic shortcomings. As the primary (evolved) component is more important to our conclusions, and the models do not have such a problem in explaining this component, we still use these models in interpreting this object, but loosen our criterion and compare the fits in a relative sense. Therefore, we discuss all solutions that have give $\chi'^2 < 10$. We find a best-fit of $\chi'^2 = 5.6$, which gives ($T_E = 0.5$ Gyr, $\tau_E = 0$, $M_E = 3.4 \times 10^{10} M_\odot$, $E(B - V)_E = 0$) and ($T_Y = 0.001$ Gyr, $M_Y = 2.3 \times 10^8 M_\odot$, $E(B - V)_Y = 0$), respectively. Both components have solar metallicity.

(I) Solutions of $\chi'^2 < 10$ can only be found when the young component has $T_Y \leq 30$ Myr and $E(B - V)_Y = 0$. Similar to the case of #5abc, we have no constraint on the SFH of this component.

(II) If we require the primary component have the same reddening as the secondary one, *i.e.*, $E(B - V)_E = 0$, we have following constraints on the primary component:

(1) τ & T : Solutions of $\chi'^2 < 10$ can only be found when $T_E \geq 0.2$ Gyr and $\tau_E \leq 0.6$ Gyr. The minimum T_E of 0.2 Gyr implies a formation redshift $z_f \gtrsim 7$. If $0.5 \leq \tau_E \leq 0.6$ Gyr, solutions of comparable quality can only be found at $T_E \geq 0.8$ Gyr, which means $z_f \gtrsim 20$.

(2) M : Solutions of $\chi'^2 < 10$ can only be found within $1.4 \times 10^{10} \leq M_E \leq 5.7 \times 10^{10} M_\odot$.

(3) Z : While we see the general trend of worsening fit with decreasing metallicity, we are not able to reject models with lower metallicities. However, we point out that if

⁷This object is one of the objects discussed by Eyles et al. (2005). Our main results broadly agree with theirs in the sense that the best-fit stellar mass is $> 10^{10} M_\odot$ and the age is a few hundred Myrs.

$Z = 1/200Z_{\odot}$, the only $\chi'^2 < 10$ solutions available are those having very old T_E (≥ 0.8 Gyr) and very short τ_E (very close to SSPs).

(III) Allowing $E(B - V)_E$ to be different from $E(B - V)_Y$ makes the models largely unconstrained. However, we find that $E(B - V)_E$ cannot be larger than 0.4 mag (for the same reason as in the case of #5abc) and M cannot be less than $2.0 \times 10^{10} M_{\odot}$, or no solution of $\chi'^2 < 10$ can be found.

The SED analysis for these $z \approx 6$ objects, especially #1ab and 5abc, strongly suggests that systems as massive as $M \sim 10^{10} M_{\odot}$ already existed when the universe was less than 1 Gyr old, and they probably started forming their stars several hundred Myr earlier. While we do not have a strong constraint on their metallicities, they are consistent with solar abundance, implying that they might have already been significantly polluted by metals. Dust reddening to the three objects in our sample seems to be moderate or even negligible, and the best-fits to their SEDs always have zero reddening. Dust with grayer attenuation could, however, cause extinction without reddening. This would also increase the stellar masses derived for the galaxies.

5.2. Very blue rest-frame UV colors and hint of very massive stars

As mentioned above, #1ab has an abnormally blue ($z_{850} - J_{110}$) color as compared to the BC03 models⁸. Such a very blue rest-frame UV color is not unique to this object, however. In fact, most of the $z \approx 6$ candidates in YW04 that have NICMOS photometry show such a trend in their ($z_{850} - J_{110}$) colors, some of which even have ($z_{850} - J_{110}$) ~ -0.5 mag (see Fig. 1 of YW04; see also Stanway et al. 2004). The matched-aperture photometry described in §3.3 further confirms this result, and gives more accurate measurements of the colors. No matter what the specific SFH is, a galaxy at this redshift should have a rather flat SED (in terms of f_{ν} vs. λ) in the rest-frame UV, i.e., its ($z_{850} - J_{110}$) colors should be close to zero. The NICMOS J_{110} bandpass heavily overlaps that of the ACS z_{850} bandpass, making it quite difficult to produce colors as blue as those observed here.

Fig. 4 compares the measured ($z_{850} - J_{110}$) colors of the $z \approx 6$ galaxies that have NICMOS photometry against the expected ($z_{850} - J_{110}$) colors as a function of redshift as derived from a series of solar metallicity models. The models are drawn from those mentioned in §4, and are of four types of representative SFH: SSP, $\tau = 0.1$ Gyr, $\tau = 1.0$ Gyr, and

⁸The discrepancy is not likely caused by a zeropoint error in J_{110} , as the zeropoints in the NICMOS passbands are accurate to 0.01–0.02 mag (R. Thompson, private communication).

constant star-formation. The ages of the models are 0.001 Gyr, 0.01 to 0.09 Gyr (0.01 Gyr step-size), and 0.1 to 1.1 Gyr (0.1 Gyr step-size). The youngest track is at the bottom, and the oldest track is at the top. The three IRAC-detected sources are shown as filled squares: #1ab is put at $z = 5.83$ without a redshift error bar, #5abc is put at $z = 6.0$ with an uneven error bar from $z = 5.9$ to 6.4 , and #7ab is put at $z = 6$ with an error bar indicating its possible redshift range of $5.5 \leq z \leq 6.5$. The open squares (all put at $z = 6$ and with error bars from $z = 5.5$ to 6.5) are other $z \approx 6$ objects that have NICMOS photometry.

While object #7ab can be explained reasonably well by a population with age of ~ 0.1 Gyr, the majority of the sources are problematic. Regardless of the SFH, the bluest color “boundary” is always defined by the zero-age track (almost indistinguishable from the 0.001Gyr track in the figure), which cannot extend to $(z_{850} - J_{110}) < -0.2$ mag at any redshift. We emphasize that object #1ab, whose redshift is unambiguously known, is not consistent with any of these models. Such blue colors cannot be attributed to low metal abundance, as the most metal-poor (1/200 of solar, or $Z = 0.0001$) models of BC03 have essentially the same bluest color boundary as shown in Fig. 4. A less severe intervening HI absorption than that of Madau (1995) might possibly explain the bluer colors at $z \geq 6$ if $(z_{850} - J_{110}) > 0$ mag, but cannot explain the $(z_{850} - J_{110}) < -0.2$ mag colors at $z < 6$. Another possibility would be the presence of a strong Ly α emission line in the z_{850} band, which could make the $(z_{850} - J_{110})$ color bluer than the models predict. In order to reproduce the observed colors of #1ab, however, the Ly α line would have to have rest-frame equivalent width (EW) $> 300\text{\AA}$. This is not the case for #1ab; we examined its spectrum obtained at the Keck (Dickinson et al. 2004), and found that it only had a moderately strong Ly α line with rest-frame EW=18 \AA . Neither is it the case for the major component of #5abc, which do not show Ly α emission line based on the grism spectra of the GRAPES program.

These very blue rest-frame UV colors might suggest that our model templates do not sufficiently populate the entire parameter space. One limitation of the BC03 models is that the high-mass end of the adopted Salpeter IMF cuts off at $100 M_{\odot}$. If more massive stars are included, such very blue colors could be explained. For example, a toy galaxy model consists of only the hottest stars ($T_{eff} \sim 30,000K$; solar metallicity) from Lejeune et al. (1997) can easily explain the observed $(z_{850} - J_{110})$ colors. The lifetime of such very hot (thus very massive) stars, however, is very short (in any case $< 1Myr$), which indicates that we might be watching a special episode when these early galaxies were actively forming the most massive stars.

As varying the IMF of the BC03 models is beyond the scope of this paper, here we still adopt these models as they are, but caution that the SED fitting based on these models will likely have problems in explaining the rest-frame UV part of some of the SEDs. In

spite of this drawback, one conclusion seems inescapable from this analysis is that most galaxies shown in Fig. 3 (including #1ab and #5abc) have young components indicative of very recent (≤ 30 Myr) star formation. Furthermore, the dust reddening in these young components is likely minimal, otherwise their intrinsic rest-frame UV colors would be even bluer and more difficult to explain.

6. Stellar populations at $z \approx 5$

In this section, we discuss in detail the fitting results for the $z \approx 5$ objects. The passbands that go into the fitting process are from V_{606} to $4.5\mu m$. The best-fit models are shown in Fig. 5 and 7, and their parameters are summarized in Tab. 4.

6.1. SED fitting results

We first consider the five objects that have NICMOS photometry.

Object #6ab ($z = 4.65$): This object can be well explained by single-component models. As its redshift is known, with its 8 bands of photometry the degrees of freedom are $\nu = 3$. Thus our criterion of high-quality is $\chi'^2 \leq 1.82$. While high-quality solutions are available at all metallicities, the goodness-of-fit improves with smaller Z values. The best-fit has $\chi'^2 = 0.45$, and has ($T = 1.3$ Gyr, $\tau = 0.4$ Gyr, $M = 2.8 \times 10^{10} M_{\odot}$, $E(B - V) = 0$, $Z = 1/200Z_{\odot}$). We find high-quality solutions only within the following ranges: $E(B - V) \leq 0.23$ mag, $\tau \geq 0.2$ Gyr, $T > 0.5$ Gyr, and $1.8 \times 10^{10} \leq M \leq 5.1 \times 10^{10} M_{\odot}$. The lower bound of its age implies $z_f \gtrsim 7.3$.

Object #15ab ($z = 5.49$): Our models (either single-component or two-component) cannot produce any fit with $\chi'^2 < 40$ for this object because of its abnormally blue ($i_{750} - z_{850}$) color. As discussed in previous section, such an abnormal color of this object in particular could be explained by a less severe HI absorption in the IGM along the sight-line. If we exclude the i_{775} band from the fitting process based on the argument that our knowledge about the IGM HI absorption is imperfect, we can find high-quality fits using single-component models. The best-fit has $\chi'^2 = 1.63$, and gives ($T = 1.0$ Gyr, $\tau = 0.6$ Gyr, $M = 2.2 \times 10^{10} M_{\odot}$, $E(B - V) = 0$, $Z = Z_{\odot}$). We find no high-quality solutions unless $E(B - V) = 0$. On the other hand, we have no obvious constraint on its metallicity. High-quality solutions are available if $0.3 \leq \tau \leq 0.7$ Gyr, $0.8 \leq T \leq 1.0$ Gyr, and $1.8 \times 10^{10} \leq M \leq 3.6 \times 10^{10} M_{\odot}$. The age range implies that the formation redshift of this object is likely $z_f \gtrsim 15.8$. Rhoads et al. (2005) considered whether this object could be powered by an active galactic nucleus

(AGN), but did not reach a conclusive answer. We do not find any compelling evidence in its SED that this object harbors an AGN.

Object #48ab: Regardless of the values of other parameters, the photometric redshift of this object is well constrained at $z_p = 5.2$. The best single-component fit to this object gives $\chi'^2 = 2.48$, which does not strictly satisfy our high-quality criterion ($\chi'^2 = 2.41$ in this case). The parameters of this fit are ($T = 0.03$ Gyr, $\tau = 0$, $M = 9.4 \times 10^8 M_\odot$, $Z = 1/5 Z_\odot$, $E(B - V)_E = 0$). The large χ^2 of this best-fit comes mostly from the discrepancy in the IRAC $3.6\mu\text{m}$ band, where the model is lower than the observation by a factor of six.

Thus we also explore two-component models. We find the following:

(1) High-quality fits can be obtained only when $E(B - V)_Y = 0$. If we limit the reddening of the primary component also to $E(B - V)_E = 0$, the fit only improves moderately. The best-fit ($\chi'^2 = 1.82$) has a metallicity of $Z = 0.4 Z_\odot$, and has ($T_E = 1.0$ Gyr, $\tau_E = 0$, $M_E = 1.2 \times 10^{10} M_\odot$) and ($T_Y = 10$ Myr, $\tau_Y = 0$, $M_Y = 2.2 \times 10^8 M_\odot$).

(2) If we allow non-zero $E(B - V)_E$, very high-quality fits ($\chi'^2 \lesssim 0.3$) can be obtained. However, parameters of these fits span vastly different ranges and thus are not constrained. For example, the fitted stellar mass M_E can be arbitrarily high with increasingly severe reddening. Its age is also arbitrary with different reddening values, spanning from 10 Myr to 1.0 Gyr.

Therefore, we consider the fit to this object uncertain at this point.

The best-fit models of the above three objects are shown in Fig. 5. The remaining two objects that have NICMOS photometry, #4ab ($z = 5.05$) and 7ab ($z = 4.78$), cannot be fitted by any models (single- or two-component) that we considered. The discrepancy between the models and the observations is mainly in the rest-frame UV, which is very likely a problem intrinsic to the current BC03 models (for example, the cut-off at the high-mass end of the adopted IMF) rather than a problem that can be attributed to more complicated SFH.

Objects without NICMOS photometry can all be well-fitted by single-component models. As we do not have J_{110} and H_{160} bands that are critical in determining the rest-frame UV slope and UV-to-optical slope, the parameters (except their photometric redshifts, which are largely determined by their $V_{606} - i_{775}$ colors) are not tightly constrained for most objects. The details of the fits to these objects are given below. Object #18 is completely unconstrained the model fitting. It has comparatively red colors in both $V_{606} - i_{775}$ and $i_{775} - z_{850}$, suggesting that it may lie near the upper end of the redshift range for the $z \approx 5$ color selection. With a very blue ($z_{850} - m(3.6\mu\text{m}) = 0.13$), it is difficult to further constrain

the stellar population parameters of the object in the absence of additional near-infrared photometry. While this object is not further discussed here, its SED is shown in Fig. 8 for completeness.

Object #10: The best-fit ($\tilde{\chi}^2 = 0.51$) to this object has ($z_p = 5.2$, $T = 0.4$ Gyr, $\tau = 0.2$ Gyr, $M = 9.8 \times 10^9 M_\odot$, $E(B - V) = 0$, $Z = Z_\odot$). High-quality solutions can be found if ($E(B - V) \leq 0.23$ mag, $T \geq 20$ Myr, $1.1 \times 10^9 \leq M \leq 4.8 \times 10^{10} M_\odot$). However, we do not have any constraint on either Z or τ .

Object #13: This object has a best fit of $\tilde{\chi}^2 = 1.0$ with parameters of ($z_p = 4.7$, $T = 1.3$ Gyr, $\tau = 0.4$ Gyr, $M = 1.8 \times 10^{10} M_\odot$, $E(B - V) = 0$, $Z = 1/200 Z_\odot$). High-quality solutions are available only when ($Z < Z_\odot$, $E(B - V) \leq 0.23$ mag, $T > 0.5$ Gyr, $\tau \geq 0.2$ Gyr, $0.8 \times 10^9 \leq M \leq 3.8 \times 10^{10} M_\odot$).

Object #14ab: The best-fit to this object has $\tilde{\chi}^2 = 0.11$, and its parameters are ($z_p = 4.5$, $T = 0.7$ Gyr, $\tau = 0.2$ Gyr, $M = 2.1 \times 10^{10} M_\odot$, $E(B - V) = 0$, $Z = Z_\odot$). High-quality solutions can only be found when ($E(B - V) \leq 0.23$ mag, $0.09 \leq \tau \leq 0.8$ Gyr, $T \geq 80$ Myr, $1.3 \times 10^{10} \leq M \leq 7.8 \times 10^{10} M_\odot$). However, we do not have constraint on its metallicity.

Object #20: This object can also be very well fitted. The best-fit has $\tilde{\chi}^2 = 0.14$ with parameters of ($z_p = 4.9$, $T = 0.9$ Gyr, $\tau = 0.7$ Gyr, $M = 3.7 \times 10^9 M_\odot$, $E(B - V) = 0$, $Z = 1/200 Z_\odot$). However, we do not have any constraint on either T or τ , as high-quality solutions can be found at any values. The metallicity is also unconstrained, but there is evidence that the goodness-of-fit improves towards lower Z . The estimate on stellar mass spans a wide range, from 5.0×10^8 to $1.0 \times 10^{10} M_\odot$. The only tightly constrained parameter is the amount of reddening, for which we find $E(B - V) \leq 0.23$ mag in order to find high-quality solutions.

Object #51abcde: The best-fit to this rich group has following parameters: ($z_p = 4.6$, $T = 1.0$ Gyr, $\tau = 0.4$ Gyr, $M = 1.0 \times 10^{10} M_\odot$, $E(B - V) = 0$, $Z = 1/200 Z_\odot$). We do not have constraint on either τ or Z , but find that the goodness-of-fit improves towards lower Z . We can find high-quality solutions only if ($E(B - V) \leq 0.23$ mag, $T \geq 50$ Myr, $2.0 \times 10^9 \leq M \leq 2.2 \times 10^{10} M_\odot$).

The analysis above also shows that galaxies with stellar masses of order $M \sim 10^{10} M_\odot$ existed at $z \approx 5$, and that they likely formed at much earlier epochs. Similar to the $z \approx 6$ objects, the reddening in these $z \approx 5$ galaxies is moderate or even negligible. While the fits to the SEDs of a number of galaxies show a trend of improved quality towards lower metallicities (counter-intuitively as compared to the results in the $z \approx 6$ sample), they are all consistent with solar abundance.

6.2. Blue rest-frame UV colors in the $z \approx 5$ sample

Similar to the case of the blue rest-frame UV colors in the $z \approx 6$ sample discussed in §5.1, we find that all the $z \approx 5$ objects have blue ($i_{775} - z_{850}$) colors indicative of recent star-formation, and that some of them also have abnormally blue ($i_{775} - z_{850}$) colors that are hard to explain even the zero-age models of BC03. This is illustrated in Fig. 6, where the observed data points are superposed on the “isochrone” tracks like those shown in Fig. 3. The four objects with confirmed redshifts are the squares without horizontal error bars, while the remaining objects have redshift error bars indicating a possible range of $4.5 \leq z \leq 5.5$.

The objects that have the largest deviations from the models are #4ab and #15ab, which are at $z = 5.01$ and 5.49 , respectively. The discrepancies, however, are different for these two objects, and might represent two different mechanisms. Object #4ab deviates from the models similarly to the object #1ab in the $z \approx 6$ sample, and such a discrepancy might be due to the high-mass end cut-off of the IMF adopted by BC03. The blue color of object #15ab, on the other hand, cannot be explained in this way. Although it might be reproduced if the galaxy redshift were significantly smaller, we note (§3.4) that the redshifts from both Keck and the GRAPES ACS grism spectrum agree very well ($z = 5.40$ and 5.52 , respectively), so we consider this explanation unlikely. Given its redshift, its intrinsic UV emission in the i_{775} -band, no matter how strong it is, would be easily quenched by the Ly α absorptions of the IGM HI clouds along the sight-line. The fact that its observed i_{775} -band flux is much stronger than expected suggests that the IGM HI absorption along this particular sight-line might not be as strong as what Madau (1995) prescribed. If we keep the absorption scheme of Madau (1995), the photometric redshift for this object would be well constrained at $z_p = 4.60$ instead of the spectroscopic redshift $z = 5.49$. A toy model that offers the simplest explanation to its observed color, therefore, is that the distribution of the IGM HI clouds still follows the law of Madau (1995) all the way to $z \approx 4.6$, but there are very few HI clouds from $z \approx 4.6$ to 5.49 . We emphasize that such a toy model might not be physical, and that a plausible model should wait until sufficiently high S/N, high resolution spectrum is available for this object.

7. The number density of massive galaxies at $z \approx 5$ to 6

The analysis presented here shows that galaxies with stellar masses $M \gtrsim 10^{10} M_\odot$ existed at $z \approx 5$ to 6, when the universe was only ~ 1 Gyr old. Moreover, some of those galaxies appear to have been forming stars for several hundred Myr, beginning at quite large redshifts, $z \approx 7$ to 20. Eyles et al. (2005) derived similar properties for the two $z \approx 6$ galaxies that they analyzed. The stellar masses of these galaxies are similar to those that have been estimated

for typical (“ L^* ”) Lyman break galaxies at $z \approx 3$ (Papovich et al. 2001), when the universe was roughly twice as old as it was at $z \approx 5$ –6. As we have noted in §3.1, the high- z galaxies that are detected by IRAC are also among the optically brightest star-forming galaxies at these redshifts, and thus may be at the upper end of the mass function, although this has yet to be properly quantified. We may ask, however, if the existence of objects with these masses is consistent with predictions from models of galaxy formation in a Λ -dominated cold dark matter (Λ CDM) universe. There has been a lively debate in the literature as to whether such models can reproduce the observed number density and stellar population properties of massive galaxies at lower redshifts ($z \approx 1$ to 3, e.g., Fontana et al. 2003; Poli et al. 2003; Nagamine et al. 2004; Somerville et al. 2004). While our HUDF+IRAC sample is not complete in any sense, it is still useful to compare the lower limits on massive galaxy space density thus derived against the models in order to extend these tests to earlier cosmic times.

For this purpose, we compare our data to recent hydrodynamic simulations in a Λ CDM universe as described in Nagamine et al. (2004) and Night et al. (2005). Those authors kindly provided us with mass functions from two types of simulations, namely, a Smoothed Particle Hydrodynamics (SPH) simulation and a Total Variation Diminishing (TVD) simulation. The SPH model simulates a co-moving volume nearly 100 times larger than that of the TVD model (box sizes of $100h^{-1}$ Mpc and $22h^{-1}$ Mpc, respectively), and therefore provides better statistics for rarer, high mass objects. In the mass range of overlap, however, and before resolution effects limit the SPH simulation, the TVD model predicts roughly two to three times as many galaxies per unit volume at fixed stellar mass.

Our galaxy sample is by no means complete due to the fact that we have considered only objects that were reasonably isolated in the IRAC images and therefore whose detection and photometry was not subject to blending issues. We may nevertheless estimate the stellar mass limit at which our sample should be complete, modulo IRAC crowding. We have not rigorously quantified the effects of incompleteness. However, in §3.1 we have noted that this relatively isolated, IRAC-detected subsample makes up about one third of the total number of galaxies in each color-selected sample range down to the ACS magnitude limits of 26.9 in z_{850} (for $z \approx 6$) or i_{775} (for $z \approx 5$), and that only a few of the other two-thirds fraction not analyzed here are clearly *undetected* in the IRAC data. We infer, therefore, that the incompleteness correction in the IRAC-detected sample is unlikely to be more than a factor of ~ 3 .

As described in §3.1, object detection in IRAC was done on the weighted sum of the $3.6\mu\text{m}$ and $4.5\mu\text{m}$ images. The $3.6\mu\text{m}$ data are deeper and contribute most of to the signal-to-noise ratio of this sum, and therefore we consider that band only for the IRAC detection limit.

While the formal $S/N = 5$ point source limit of the GOODS IRAC data is $m_{3.6\mu m} = 26.4$ mag, we will adopt a brighter $S/N = 10$ limit $m_{3.6\mu m} = 25.65$ mag for the present analysis, where detection and photometry are more secure, and where the effects of crowding and incompleteness are reduced. All but one of the galaxies in the subsample for which we have derived mass estimates (#20 at $z_p = 4.9$) are brighter than this limit. For the redshift range covered by the ACS color selection (roughly $4.5 \leq z \leq 6.5$), the $3.6\mu m$ band measures rest-frame light in the $0.48\text{--}0.65\mu m$ rest frame wavelength range, i.e., on average around the rest-frame V -band. Galaxies in the sample must have sufficient ongoing star formation to produce the UV light which allows them to be detected by ACS. Their ages, star formation histories, and dust content result in different stellar mass-to-light ratios (M/L). In practice, for the stellar population models which best fit the objects in our sample, we find $0.17 < M_*/L_V < 0.66$ in solar units. The upper bound is not far from the maximum M/L_V that we would expect for an unreddened stellar population at this redshift, given the age of the universe (1 Gyr at $z = 5.8$, yielding $(M/L_V)_{max} = 0.77$). Therefore, we adopt the upper bound of the model-fit M/L range as appropriate for the sort of UV-selected objects in this sample, but it would make little difference to use the maximum allowable M/L . At $z = 6.5$, for this upper bound to M/L , our adopted IRAC magnitude limit corresponds to a stellar mass limit of $1.6 \times 10^{10} M_\odot$. We therefore expect to be able to detect any galaxy above this mass limit in the IRAC data at these redshifts, and we adopt this threshold for comparison to the models.

To calculate the effective volumes over which we identify galaxies in our sample, we use the solid angle of the HUDF, and the redshift selection function for our color criteria (§2), which we evaluate from Monte Carlo simulations following the procedures described in Giavalisco et al. (2004b). We selected galaxies within the clean area of the ACS HUDF image that remains after trimming off the noisy edges, and which subtends 10.34 arcmin^2 . In the Monte Carlo simulations, artificial galaxies with realistic distributions of UV rest-frame colors, sizes, and magnitudes, and spanning the range of redshifts of interest, were added to the real HUDF ACS images and recovered with SExtractor. The fraction of input objects that are recovered and which meet the color selection criteria, as a function of redshift, gives the redshift selection function, which we then integrate to get the effective volume for the sample. Within the HUDF solid angle, our selection criteria correspond to effective survey volumes of $2.5 \times 10^4 \text{ Mpc}^3$ and $2.8 \times 10^4 \text{ Mpc}^3$ for the $z \approx 6$ and $z \approx 5$ samples, respectively.

We use the best-fit stellar masses for the galaxies we have analyzed, as reported in Tables 3 and 4. In the $z \approx 6$ sample, there are two galaxies (out of three total) with $M > 1.6 \times 10^{10} M_\odot$, corresponding to a space density of $0.8 \times 10^{-4} \text{ Mpc}^{-3}$ for this mass range. In the $z \approx 5$ sample, there are four galaxies (out of eight with derived masses) with $M > 1.6 \times 10^{10} M_\odot$, or a space density of $1.4 \times 10^{-4} \text{ Mpc}^{-3}$. For comparison, at $z = 6$,

the SPH and TVD simulations give cumulative number densities of $2.1 \times 10^{-4} \text{ Mpc}^{-3}$ and $3.7 \times 10^{-4} \text{ Mpc}^{-3}$, respectively, or 2.6 and 4.6 times larger than the observed number. At $z = 5$ the number densities in the models are $9.0 \times 10^{-4} \text{ Mpc}^{-3}$ and $18.6 \times 10^{-4} \text{ Mpc}^{-3}$, or 6.4 and 13.3 times larger than the number of galaxies in our sample above this mass threshold.

Even allowing for a generous degree of incompleteness in our sample, we conclude that Λ CDM models like those considered here can successfully produce enough galaxies at these redshifts with masses like those we have inferred. The basic nature of the result is largely insensitive to the choices we have adopted such as the IRAC magnitude limit or the maximum allowable M/L threshold, unless there were a substantial number of comparably massive galaxies with UV fluxes so faint as to be undetected in the ACS HUDF images, or, at least, not selected by our color criteria. The actual ratios of the observed to predicted number densities are, however, quite sensitive to these details, due to the very steep mass function in the simulations ($dN/dM_* \propto M_*^\alpha$, with $\alpha \approx -2.5$ in this mass range, which we note is divergent if extended to arbitrarily low masses, below the resolution of the simulations). We also note that these models predict quite steep redshift evolution in the number density of objects in this mass range (roughly a factor of 4 to 5 increase from $z = 6$ to $z = 5$). Future analysis of the GOODS *Spitzer* data should allow us to test these predictions by examining complete, infrared-selected samples that will more nearly approximate populations limited by stellar mass at different redshifts. Two ultradeep IRAC fields have also been observed in GOODS-N, which will provide additional dynamic range to help test the steepness of the mass function predicted by the simulations. Analysis of other data will also help to control the potential field-to-field variations in the observed number density that may result from clustering, which we may expect would be strong for galaxies at the upper range of the mass function at these redshifts.

8. Summary

Using the first epoch of GOODS IRAC observations, we have identified mid-infrared counterparts of the $z \approx 6$ and 5 galaxy candidates selected in the HUDF. Six of these galaxies have spectroscopic confirmation, verifying that the IRAC instrument can indeed probe galaxies to such high redshifts, and as faint as ~ 26.9 mag in the ACS z_{850} or i_{750} bands. In this paper, we study three and eleven objects in the $z \approx 6$ and 5 samples, respectively, all of which are reasonably isolated so that crowding in the IRAC images does not compromise their photometry.

Combining the photometry from ACS, NICMOS (in one occasion also ISAAC at the VLT) and IRAC, we analyze the rest-frame UV to optical spectral energy distributions of

these galaxies and compare them to stellar population synthesis models. IRAC samples redshifted rest-frame optical wavelengths where there is a greater contribution of light from intermediate-age and long-lived stars, and where the effects of dust extinction are reduced compared to those in the ultraviolet rest frame. These data therefore help us to estimate the stellar masses and ages of these galaxies. Deep near-infrared data in two passbands from NICMOS are also available for many of the objects. These provide measurements of the UV luminosity and spectral slope, which are sensitive to the on-going star formation rate and degree of dust reddening, quantities that are insufficiently constrained from the ACS optical data alone.

While the SED analysis reveals diversity in the stellar populations of these galaxies, it also demonstrates a number of common properties. The following are the most important results from this study.

(1) Galaxies as massive as $\sim 10^{10}M_{\odot}$ already existed when the universe was about a billion years old. These stellar masses are similar to those of typical (L^*) Lyman-break galaxies at $z \approx 3$, when the Universe was roughly twice as old as it was at $z \approx 5$ to 6. Two out of the three objects in the $z \approx 6$ sample, and at least four out eleven objects from the $z \approx 5$ sample, have best-fit stellar masses $M > 1.6 \times 10^{10}M_{\odot}$. While the acceptable fits to these objects span a considerable range in the stellar population model parameter space, the lower bound to their stellar masses is well constrained to be $> 10^{10}M_{\odot}$. Although the galaxy samples are incomplete, the resulting lower limits on their space density at these stellar masses can be comfortably accommodated by at least one set of recent Λ CDM models for galaxy formation (Nagamine et al. 2004; Night et al. 2005). Those models predict a very steep mass function and quite rapid redshift evolution of the number density of galaxies at fixed stellar mass, predictions which may be tested by the analysis of larger and deeper samples from the GOODS *Spitzer* data set.

(2) The photometry for most of the galaxies studied here shows evidence for a pronounced increase in flux density between the rest-frame UV wavelengths (ACS and NICMOS) and the optical light measured by IRAC. This is naturally reproduced by a Balmer break that results from the dominant presence of stars with ages of a few hundred Myr. All three $z \approx 6$ objects have best-fit ages $\gtrsim 0.1$ Gyr, while at least eight $z \approx 5$ objects have best-fit ages $\gtrsim 0.4$ Gyr. In particular, the $z \approx 6$ sample strongly indicates that the universe was already forming galaxies as massive as $\sim 10^{10}M_{\odot}$ at $z \gtrsim 7$, and possibly even at $z \sim 20$. First-year results from WMAP suggest that the reionization of the universe first began at $z \sim 15$ – 20 (Spergel et al. 2003). The stellar population properties that we derive are in qualitative agreement with this picture, demonstrating that stars, which provide an important – if not the only – source of reionizing photons, could indeed be formed at such

an early epoch.

(3) While there is no firm constraint on the metallicity of these galaxies, all the objects analyzed here are consistent with solar abundance, which indicates that the galaxies in such an early stage of the universe might have already been significantly polluted by metals. In fact, the best-fit models to all the three $z \approx 6$ objects have solar metallicity, and for one object there is strong evidence that its metallicity must be higher than $1/200Z_{\odot}$. If these metallicities are representative at $z \approx 6$, this may cast doubt on the suggestion (*e.g.*, Stiavelli et al. 2004) that extremely metal-poor galaxies could be the major sources that finished the reionization at $z \approx 6$.

(4) In all cases, the best-fit stellar population models have no dust reddening, and the allowed models generally have low extinction values. Even so, several galaxies, including three with spectroscopic confirmation, show abnormally blue rest-frame UV colors compared to these unreddened models. We find that in two cases (at $z = 5.83$ and $z = 5.05$), an IMF extending to very massive stars ($> 100M_{\odot}$), which are not included in the models used here, might account for such blue colors. This would have important implications for reionization at $z \approx 6$, offering further evidence to justify a large Lyman continuum photon escape fraction that has been adopted in a number of studies (*e.g.*, Yan & Windhorst 2004a; Yan & Windhorst 2004b). In another case (at $z = 5.49$), the blue color might be explained by a reduced degree of intergalactic HI absorption along the line of sight compared to the mean opacity predicted by Madau (1995).

The authors thanks Dr. Nagamine for providing his most recent numerical simulations. We thank the other members of the GOODS team who have contributed to the success of the observations and data analysis. We also thank the referee for very helpful comments. Support for this work, part of the *Spitzer Space Telescope* Legacy Science Program, was provided by NASA through Contract Number 1224666 issued by the Jet Propulsion Laboratory, California Institute of Technology under NASA contract 1407.

REFERENCES

- Berta, S., Fritz, J., Franceschini, A., Bressan, A., & Lonsdale, C. 2004, *A&A*, 418, 913
- Bertin, E. & Arnouts, S. 1996, *A&AS*, 117, 393
- Brinchmann, J. & Ellis, R. S., *ApJ*, 536, L77
- Bruzual, A. G. & Charlot, S. 2003, *MNRAS*, 344, 1000
- Bunker, A. J., Stanway, E. R., Ellis, R. S., & McMahon, R. G. 2004, *MNRAS*, 355, 374
- Cimatti, A., et al. 2004, *Nature*, 430, 8
- Chabrier, G. 2003, *PASP*, 115, 763
- Cohen, J. G. 2002, *ApJ*, 567, 672
- Cole, S., et al. 2001, *MNRAS*, 326, 255
- Daddi, E., et al. 2005, *ApJ*, 626, 680
- Dickinson, M., Paopvich, C., Ferguson, H. C., & Budavari, T. 2003, *ApJ*, 587, 25
- Dickinson, M., et al. 2004a, *ApJ*, 600, L99
- Dickinson, M., et al. 2004b, submitted to *ApJ*
- Drory, N., Bender, R., Snigula, J., Feulner, G., Hopp, U., Maraston, C., Hill, G. J., & de Oliveira, C. Mendes 2001, *ApJ*, 562, L111
- Egami, E., et al. 2005, *ApJ*, 618, L5
- Eyles, L., et al. 2005, submitted to *ApJ* (astro/ph-0502385)
- Fazio, G. G., et al. 2004, *ApJS*, 154, 10
- Fontana, A., et al. 2004, *A&A*, 424, 23
- Giavalisco, M., et al. 2004a, *ApJ*, 600, L93
- Giavalisco, M., et al. 2004b, *ApJ*, 600, L103
- Glazebrook, K., et al. 2004, *Nature*, 430, 181
- Labbé, I., et al. 2004, *ApJ*, 624, L81

- Nagamine, K., Cen, R., Hernquist, L., Ostriker, J. P., & Springel, V. 2004, *ApJ*, 610, 45
- Night, C., Nagamine, K., Springel, V., & Hernquist, L. 2005, submitted to *MNRAS* (astro-ph/0503631)
- Papovich, C., Dickinson, M & Ferguson, H. C. 2001, *ApJ*, 559, 620
- Pirzkal, N., et al. 2004a, *ApJS*, 154, 501
- Pirzkal, N., et al. 2004b, submitted to *ApJ*
- Press, W. H., Flannery, B. P., Teukolsky, S. A., & Vetterling, W. T. 1992, *Numerical Recipes in C: The Art of Scientific Computing*, Cambridge University Press; 2nd edition
- Rhoads, J. E. , et al. 2005, *ApJ*, 621, 582
- Sawicki, M. & Yee, H. K. C. 1998, *AJ*, 115, 1329
- Shapley, A. E., Steidel, C. C., Adelberger, K. L., Dickinson, M., Giavalisco, M., & Pettini, M. et al. 2001, *ApJ*, 562, 95
- Somerville, R. S., Lee, K., Ferguson, H. C., Gardner, J. P., Moustakas, L. A., & Giavalisco, M. 2004, *ApJ*, 600, L171
- Spergel, D. N., et al. 2003, *ApJS*, 148, 175
- Stanway, E. R., Bunker, A. J. & McMahon, R. G. 2003, *MNRAS*, 342, 439
- Stanway, E. R., McMahon, R. G., & Bunker, A. J. 2004, submitted to *MNRAS* (astro-ph/0403585)
- Stiavelli, M., Fall, S. Michael, & Panagia, N. 2004, *ApJ*, 610, 1
- Thompson, R. D., et al. 2005, accepted for publication in *AJ* (astro-ph/0503504)
- Xu, C., et al., 2005, submitted to *ApJ*
- Yan, H. & Windhorst, R., 2004a, *ApJ*, 600, L1
- Yan, H. & Windhorst, R., 2004b, *ApJ*, 612, L93 (YW04)
- Yan, H., et al. 2004, *ApJ*, 616, 63

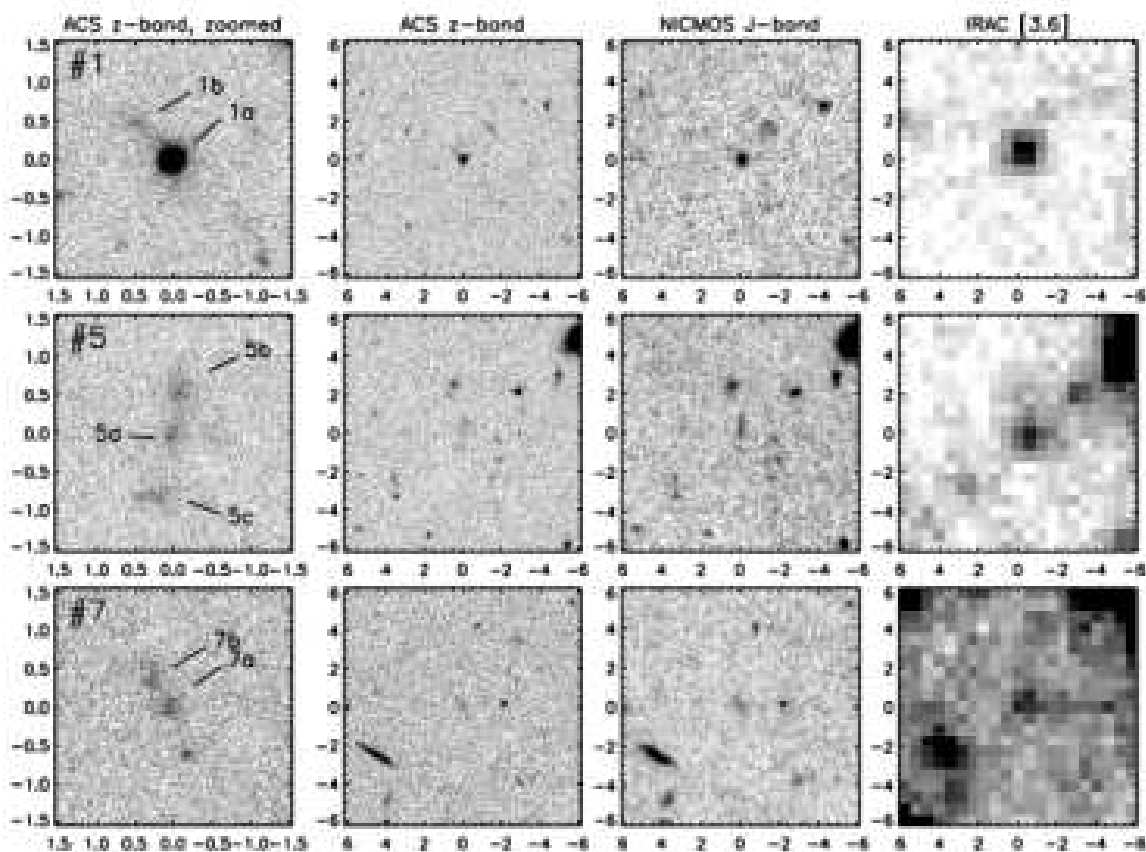


Fig. 1.— Image stamps of the IRAC-detected $z \approx 6$ objects. The ACS z_{850} -band “stamps” in the left panel are $1.5'' \times 1.5''$ in size, and show the morphological details of these objects. The images in the other three panels ($12'' \times 12''$ in size) shows the matching of these sources from ACS z_{850} to IRAC $3.6\mu m$. NICMOS J_{110} stamps are also shown when available. The ID’s of these objects are taken from YW04. Object #1ab has a spectroscopically measured redshift $z = 5.83$.

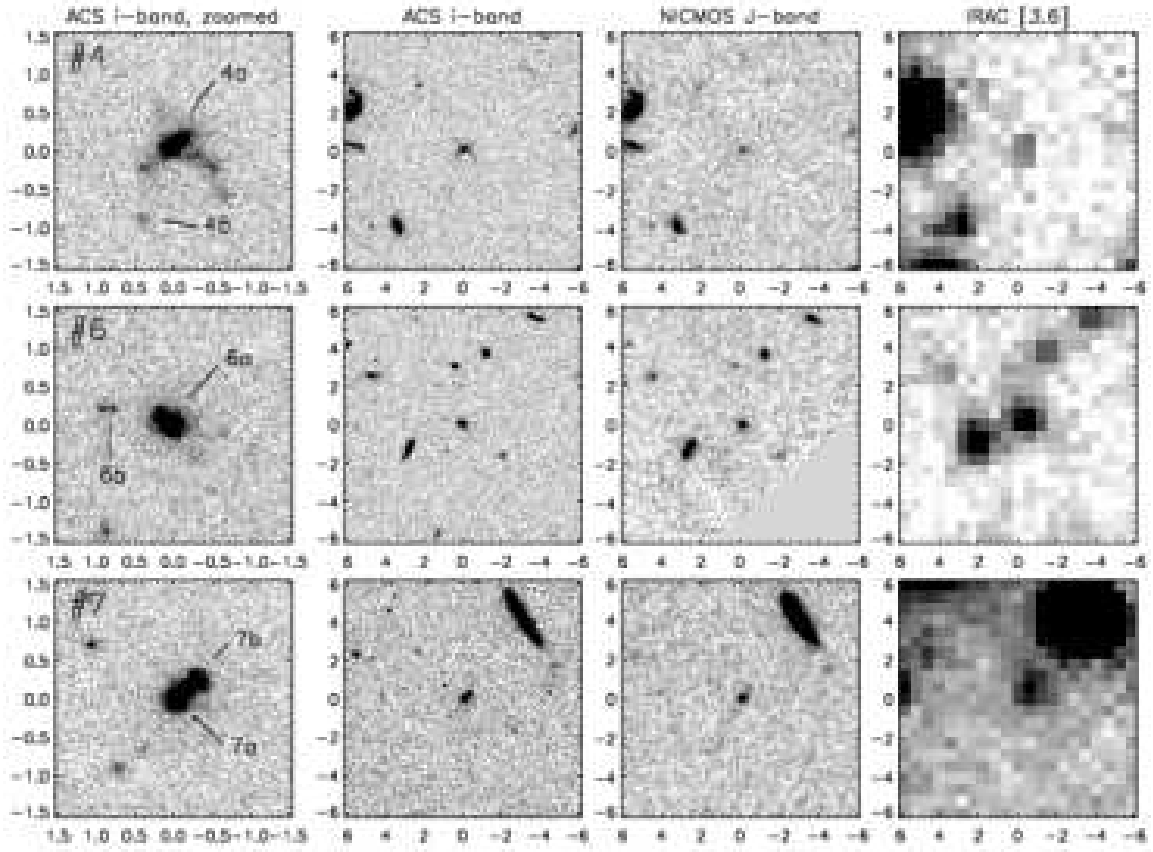


Fig. 2.— Image stamps of the IRAC-detected $z \approx 5$ objects. The ID's are taken from Yan et al. (in preparation).

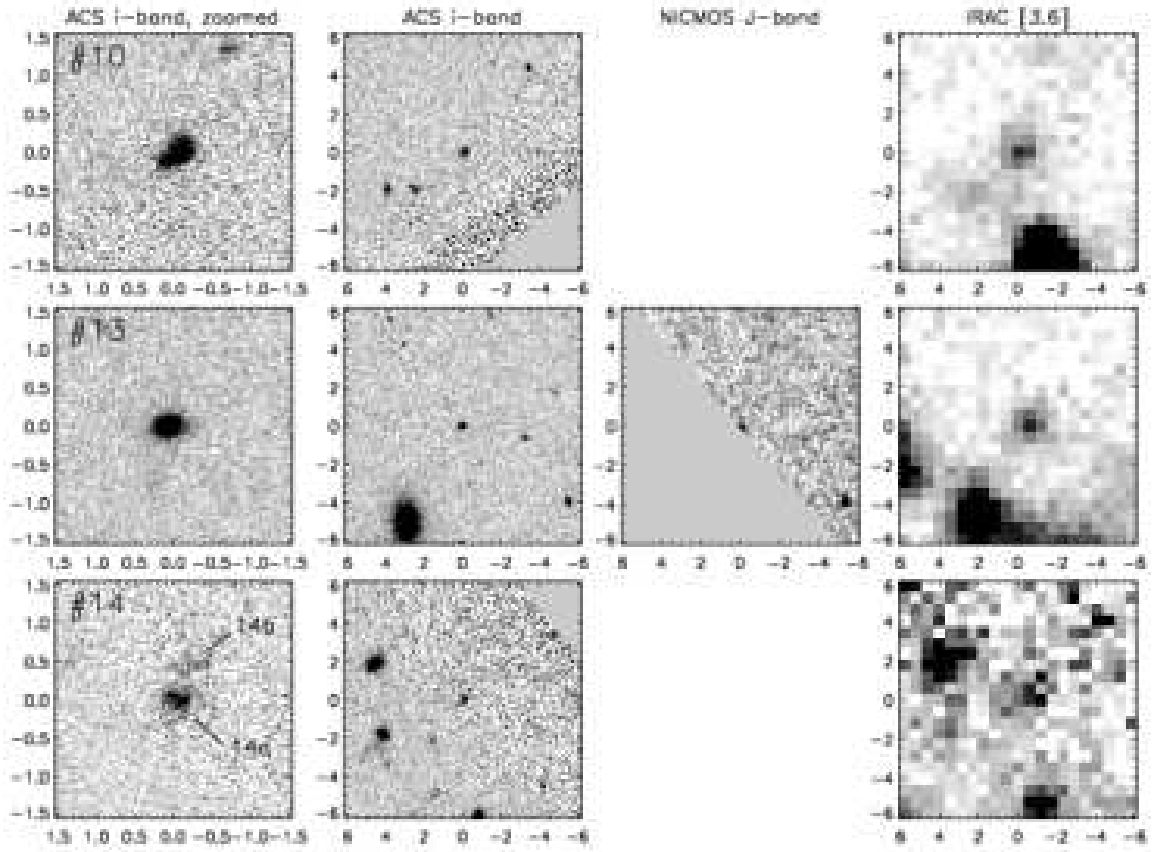


Fig. 2.— Continued.

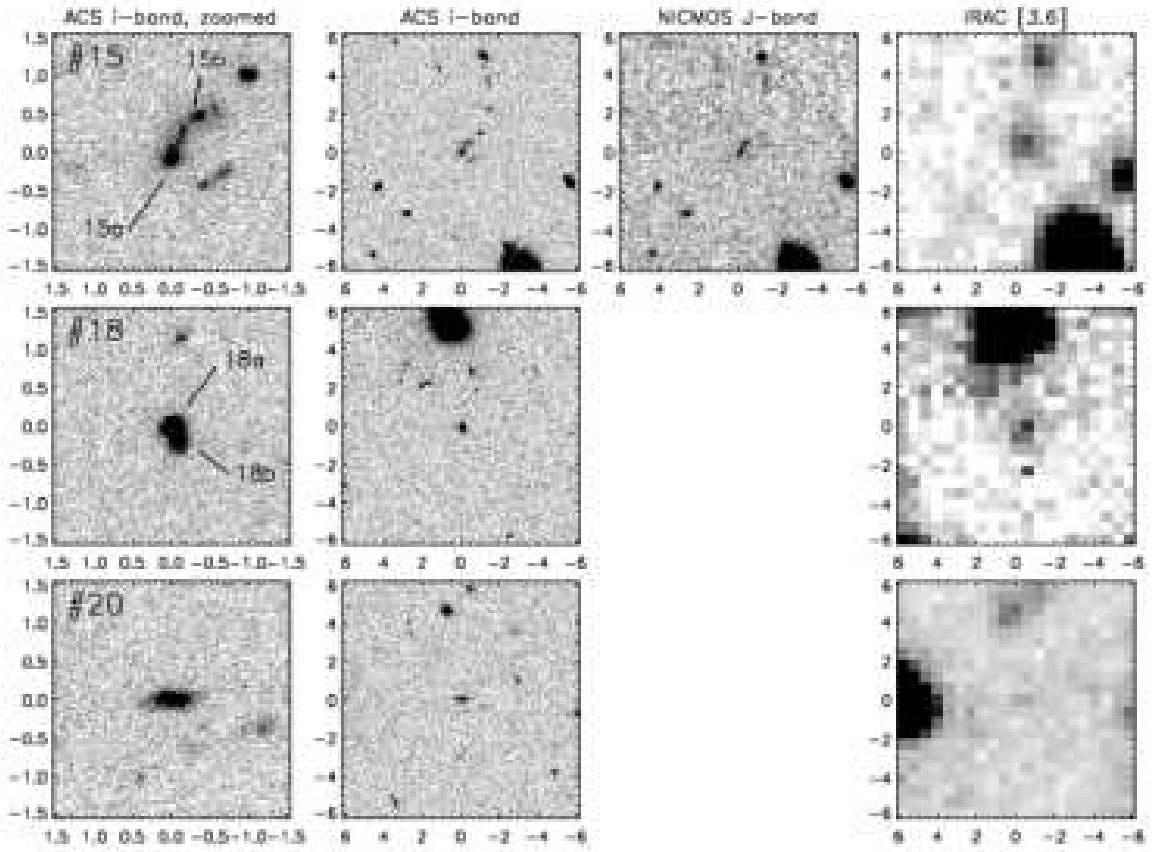


Fig. 2.— Continued.

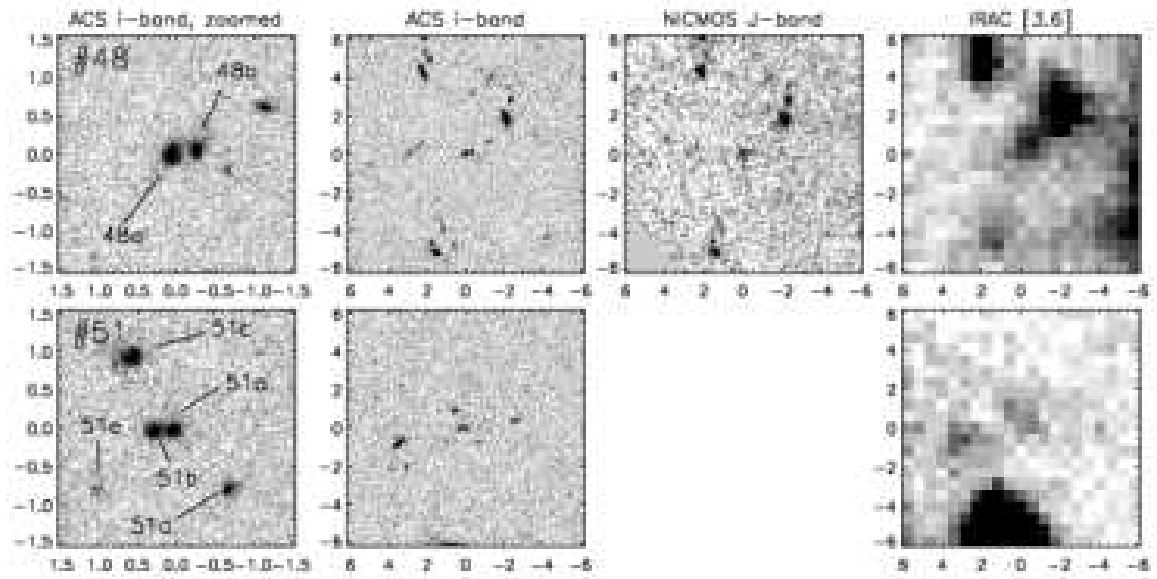


Fig. 2.— Continued.

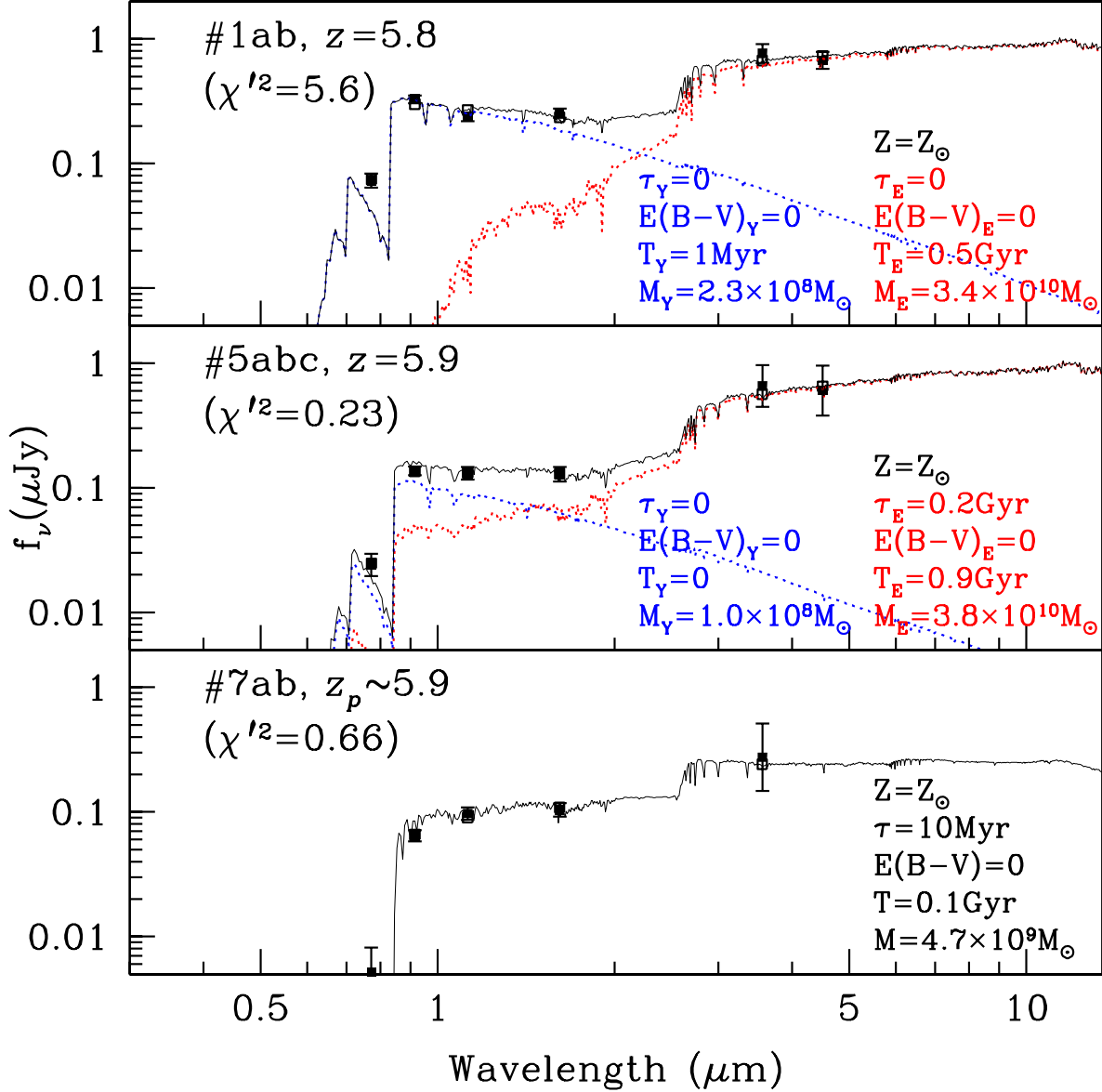


Fig. 3.— The spectra of the best-fit models to the three IRAC-detected $z \approx 6$ objects are shown in this figure. The parameters of these models are also labeled. The observed SEDs are plotted as filled squares with error bars. The model spectra are overplotted, and the synthetic model photometry integrated through the bandpasses is shown as open squares which often overlap with the filled squares. While #7ab can be explained by single-component models, both #1ab and 5abc require two-component models. For these two objects, the templates of the evolved and the young components are shown in red and blue dashed lines, respectively, and their corresponding parameters are also labeled in red and blue, respectively.

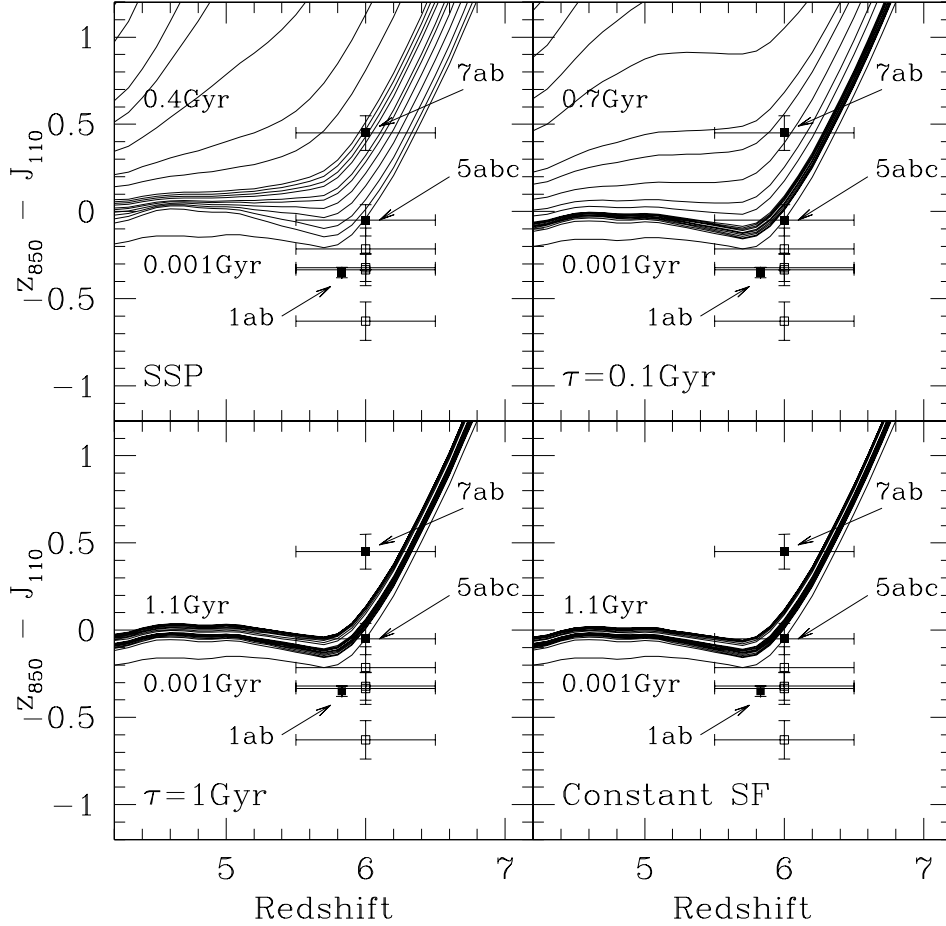


Fig. 4.— Most of the HUDF $z \approx 6$ objects that have NICMOS photometry show unusually blue ($z_{850} - J_{110}$) colors (YW04). The three that have IRAC identifications are shown here as filled squares, while the remaining ones are shown as open squares. The one without horizontal error bar is object #1ab, which has a known redshift of 5.83. The others (including #5abc; see explanation in §3.4) are put at $z = 6$ with error bars indicating their possible redshift range of $5.5 \lesssim z \lesssim 6.5$. The BC03 models are used to calculate expected colors at different redshifts and ages. Four types SFH are considered and are shown separately as the “isochrones” in each of the four panels: an instantaneous burst (SSP), continuous but declining star formation with e-folding time scales of $\tau = 0.1$ and 1 Gyr, and a constant star formation. The ages of the models are 0.001 Gyr, 0.01 to 0.09 Gyr (0.01 Gyr step-size), and 0.1 to 1.1 Gyr (0.1 Gyr step-size).

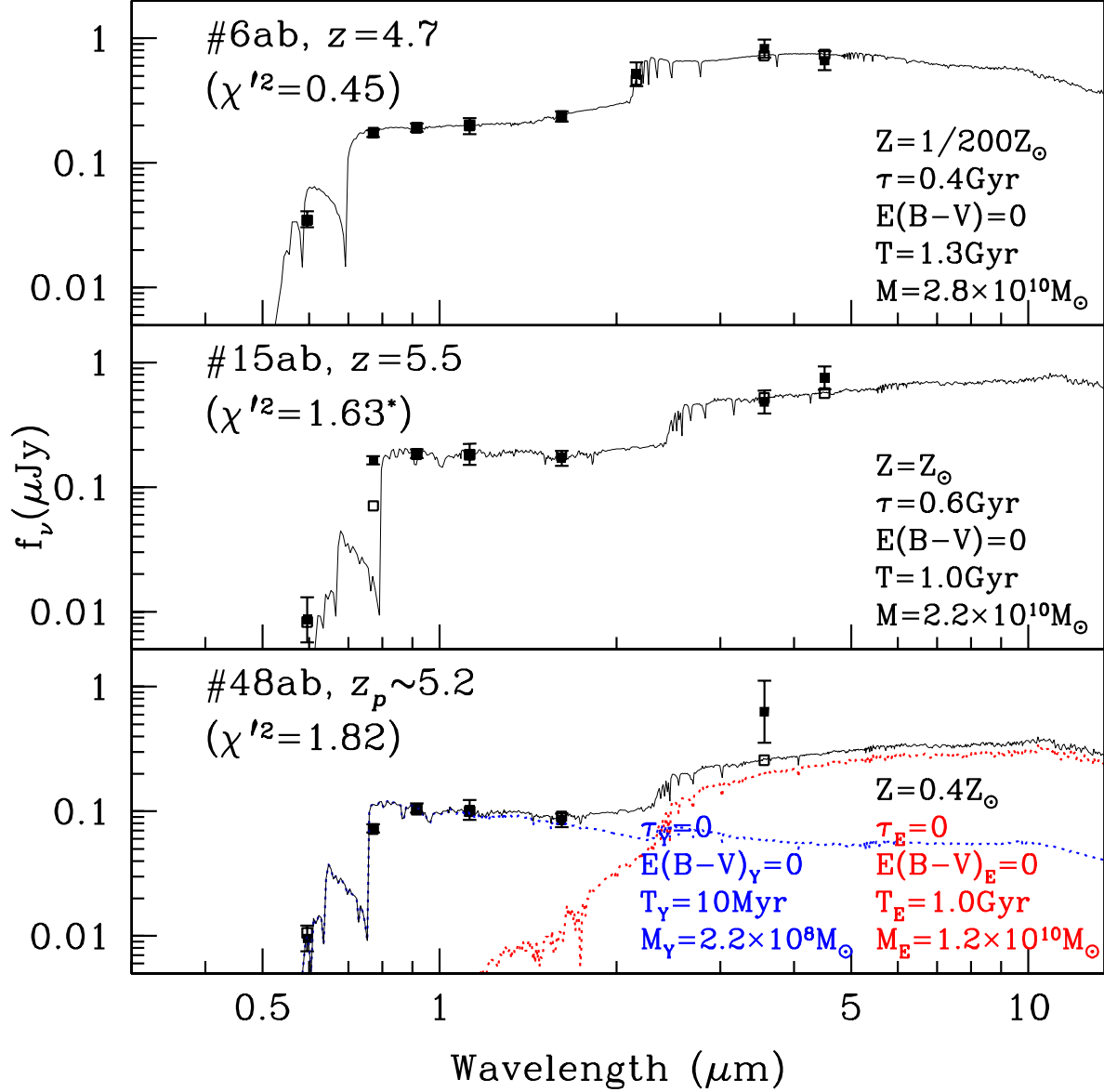


Fig. 5.— The best-fit models to the three $z \approx 5$ objects that have NICMOS photometry. Symbols are the same as in Fig. 3. Object #6ab can be well fitted by single-component models. Object #15ab, is problematic because of its abnormally blue ($i_{775} - z_{850}$) color. If we ignore i_{775} -band as justified in §6.2 (see also Fig. 6), reasonably high quality fits can be obtained using single-component models. Object #48ab, on the other hand, seems need two-component models. However, we consider the fit to this object uncertain (see §6.1 for details).

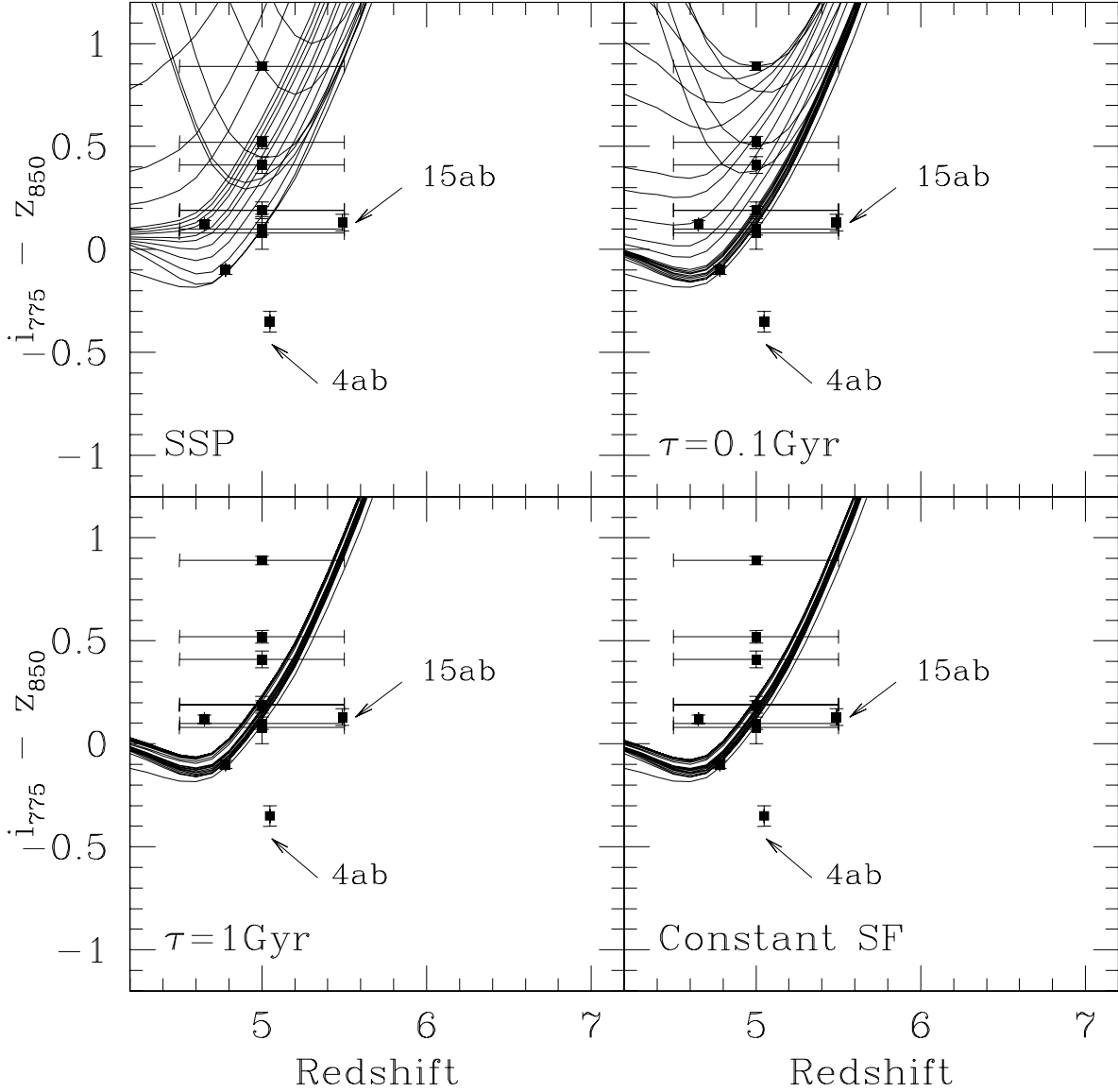


Fig. 6.— Similar to the abnormally blue rest-frame UV colors observed in some of the $z \approx 6$ candidates, a significant number of $z \approx 5$ objects in the HUDF also have blue UV colors that are inconsistent with any model. For clarity, this figure shows *only* the $z \approx 5$ objects in our sample. The “isochrone” tracks, as well as the symbols, are the same as in Fig. 4. The four objects without horizontal error bars are those that have been spectroscopically confirmed. All other objects are plotted at $z = 5$ with error bars indicating the possible redshift range of $4.5 \leq z \leq 5.5$.

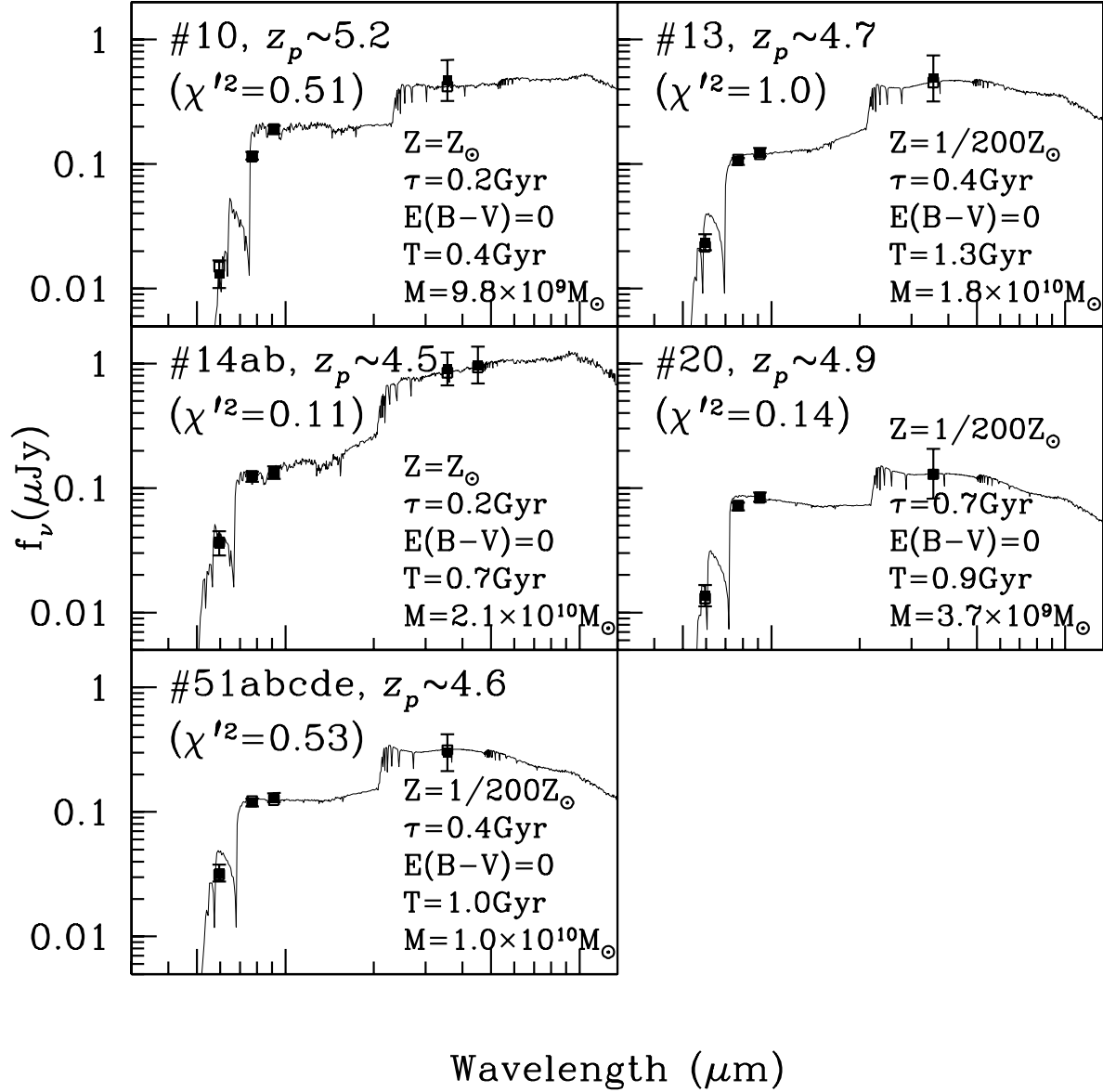


Fig. 7.— The observed SEDs of the $z \approx 5$ objects that have no NICMOS photometry are shown in this figure, with their best-fit models overplotted. The symbols are the same as in Fig. 5.

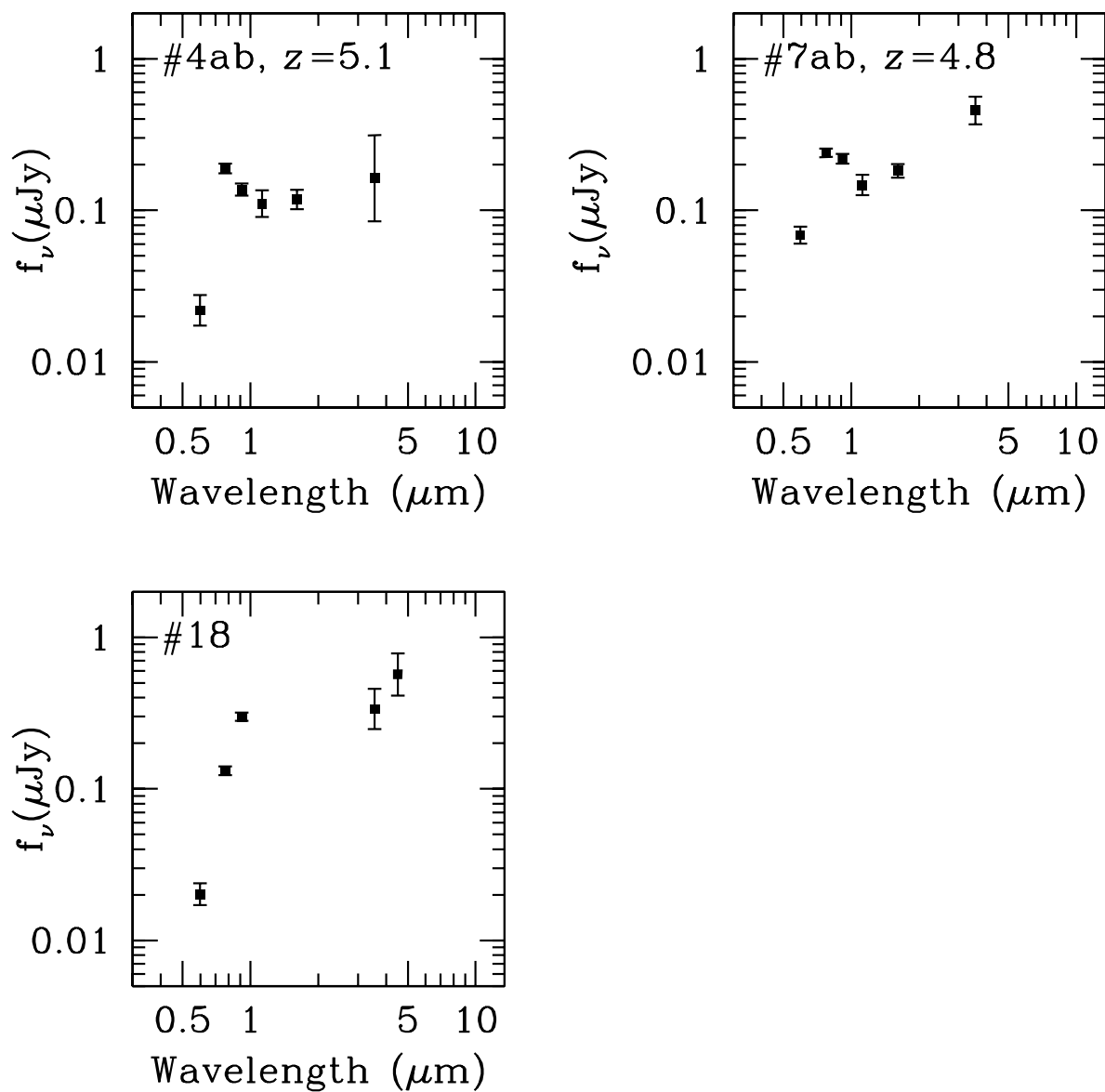


Fig. 8.— Object #4ab and 7ab in the $z \approx 5$ sample do not have good model fit. For completeness, their SEDs are shown here. Also shown is #18, which can be fitted by a large range of models and thus is unconstrained.

Table 1. Photometric properties of the IRAC-detected $z \approx 6$ objects¹

ID	RA & DEC(J2000)	i_{775}	z_{850}	J_{110}	H_{160}	$m_{3.6\mu m}$	$m_{4.5\mu m}$
1ab	...	26.74±0.14	25.11±0.08	25.46±0.09	25.39±0.10	24.19±0.19	24.33±0.17
1a	3:32:40.01 -27:48:15.01	26.88±0.03	25.25±0.01				
1b	3:32:40.04 -27:48:14.54	29.03±0.18	27.41±0.07				
5abc	...	27.95±0.23	26.06±0.09	26.11±0.13	26.13±0.15	24.36±0.42	24.45±0.50
5a	3:32:34.29 -27:47:52.80	29.07±0.21	26.97±0.05				
5b	3:32:34.28 -27:47:52.26	28.98±0.19	27.17±0.06				
5c	3:32:34.31 -27:47:53.56	29.42±0.22	27.76±0.08				
7ab	...	29.62±0.50	26.88±0.11	26.43±0.13	26.36±0.14	25.30±0.68	...
7a	3:32:37.46 -27:46:32.81	> 31.0	27.50±0.07				
7b	3:32:37.48 -27:46:32.45	29.70±0.30	27.78±0.09				

¹The combined magnitudes and photometric errors are given for these objects. These errors include the systematic errors (see §3.3). For the ACS passbands, the magnitudes and errors of individual components are also given for reference. These errors of individual components in the ACS bands are based on S/N only.

Table 2. Photometric properties of the IRAC-detected $z \approx 5$ objects¹

ID	RA & DEC(J2000)	V_{606}	i_{775}	z_{850}	J_{110}	H_{160}	$m_{3.6\mu m}$	$m_{4.5\mu m}$
4ab	...	28.05±0.25	25.71±0.08	26.06±0.10	26.29±0.22	26.22±0.16	25.87±0.71	...
4a	3:32:41.09 -27:46:42.46	28.14±0.14	25.75±0.02	26.12±0.04				
4b	3:32:41.12 -27:46:43.32	30.80±0.39	29.40±0.12	29.25±0.18				
6ab ²	...	27.53±0.16	25.81±0.07	25.69±0.08	25.66±0.16	25.47±0.10	24.11±0.18	24.35±0.19
6a	3:32:33.98 -27:48:02.05	27.63±0.05	25.88±0.01	25.73±0.02				
6b	3:32:34.04 -27:48:01.84	30.14±0.29	28.87±0.10	29.38±0.28				
7ab	...	26.81±0.14	25.45±0.07	25.55±0.08	25.98±0.17	25.75±0.11	24.75±0.23	...
7a	3:32:37.96 -27:47:11.04	27.31±0.04	25.90±0.01	26.03±0.02				
7b	3:32:37.94 -27:47:10.82	27.88±0.07	26.63±0.02	26.66±0.04				
10	3:32:31.38 -27:48:13.79	28.61±0.28	26.23±0.08	25.71±0.08	24.72±0.41	...
13	3:32:41.34 -27:48:43.09	27.97±0.16	26.35±0.07	26.16±0.08	24.68±0.46	...
14ab	...	27.51±0.24	26.17±0.10	26.09±0.13	24.01±0.33	23.93±0.37
14a	3:32:37.55 -27:45:20.59	27.83±0.14	26.46±0.05	26.38±0.07				
14b	3:32:37.52 -27:45:20.12	29.01±0.26	27.77±0.09	27.67±0.14				
15ab	...	29.06±0.45	25.86±0.08	25.73±0.09	25.74±0.21	25.82±0.15	24.69±0.23	24.21±0.23
15a	3:32:33.27 -27:47:24.94	29.45±0.34	26.50±0.03	26.26±0.04				
15b	3:32:33.24 -27:47:24.50	30.37±0.84	26.75±0.03	26.76±0.06				
18ab	...	28.14±0.18	26.10±0.07	25.21±0.07	25.08±0.33	24.51±0.35
18a	3:32:40.86 -27:45:46.19	28.76±0.09	26.67±0.02	25.83±0.01				
18b	3:32:40.86 -27:45:46.40	29.05±0.10	27.06±0.02	26.12±0.01				
20	3:32:45.25 -27:48:12.46	28.56±0.21	26.77±0.08	26.58±0.09	26.11±0.50	...
48ab	...	28.95±0.26	26.74±0.08	26.33±0.09	26.37±0.20	26.58±0.14	24.40±0.62	...
48a	3:32:45.80 -27:47:25.30	29.71±0.20	27.34±0.03	26.88±0.03				
48b	3:32:45.78 -27:47:25.26	29.69±0.23	27.67±0.04	27.34±0.05				
51abcde	...	27.63±0.17	26.21±0.08	26.11±0.09	25.21±0.37	...
51a	3:32:43.40 -27:46:26.87	28.59±0.09	27.35±0.04	27.22±0.06				
51b	3:32:43.36 -27:46:27.77	29.50±0.17	27.74±0.04	27.68±0.07				
51c	3:32:43.38 -27:46:27.80	29.11±0.11	27.75±0.04	27.61±0.06				
51d	3:32:43.31 -27:46:28.52	29.92±0.18	28.59±0.06	28.60±0.11				
51e	3:32:43.44 -27:46:28.52	31.49±0.75	29.46±0.14	29.28±0.20				

¹Similar to Table 1, but for the IRAC-identified $z \approx 5$ objects. The object IDs are taken from Yan et al. (2005, in preparation) and are independent from those of the $z \approx 6$ objects reported in Table 1.

²This objects is detected in K_s band as well: $K_s = 24.62 \pm 0.24$ mag.

Table 3. Best-fit results for the IRAC-detected $z \approx 6$ objects¹

ID ²	Redshift ³	τ_E (Gyr) ⁴	T_E (Gyr) ⁴	M_E (M_\odot) ⁴	τ_Y (Myr) ⁵	T_Y (Myr) ⁵	M_Y (M_\odot) ⁵	Metallicity (Z_\odot)	$E(B - V)$
1ab	5.83*	0	0.5	3.4×10^{10}	0	1.0	2.3×10^8	1	0
5abc	~ 5.9	0.2	0.9	3.8×10^{10}	0	0	1.0×10^8	1	0
7ab	~ 5.9	0.01	0.1	4.7×10^9	1	0

¹Parameters of the best-fit stellar population models shown in Fig. 3.

²The IDs of these multiple systems are the combination of the IDs of their individual members.

³The asterisk indicates spectroscopic redshift, while the leading \sim sign indicates photometric redshift.

⁴These values are for the major, evolved component.

⁵These values are for the secondary, young component. If these values are not present, it means the object can be explained by a single-component whose parameters are given to the left.

Table 4. Best-fit results for the IRAC-detected $z \approx 5$ objects¹

ID	Redshift	τ_E (Gyr)	T_E (Gyr)	M_E (M_\odot)	τ_Y (Myr)	T_Y (Myr)	M_Y (M_\odot)	Metallicity (Z_\odot)	$E(B - V)$
6ab	4.65*	0.4	1.3	2.8×10^{10}	1/200	0
15ab	5.49*	0.6	1.0	2.2×10^{10}	1	0
48ab	~ 5.2	0	1.0	1.2×10^{10}	0	10	2.2×10^8	0.4	0
10	~ 5.2	0.2	0.4	9.8×10^9	1	0
13	~ 4.7	0.4	1.3	1.8×10^{10}	1/200	0
14ab	~ 4.5	0.2	0.7	2.1×10^{10}	1	0
20	~ 4.9	0.7	0.9	3.7×10^9	1/200	0
51abcde	~ 4.6	0.4	1.0	1.0×10^{10}	1/200	0

¹Similar to Table 3, but for the $z \approx 5$ sources shown in Fig. 5 and 7. The top part and the bottom part (separated by the horizontal line) are for the sources with and without NICMOS measurements, respectively.